NEUROSCIENCE

A nanoparticle-based wireless deep brain stimulation system that reverses Parkinson's disease

Junguang Wu[1,2,3], Xuejing Cui[1,3]*, Lin Bao[1,3], Guanyu Liu[1,3], Xiaoyu Wang[1,3], Chunying Chen[1,2,3]*

Deep brain stimulation technology enables the neural modulation with precise spatial control but requires permanent implantation of conduits. Here, we describe a photothermal wireless deep brain stimulation nanosystem capable of eliminating α-synuclein aggregates and restoring degenerated dopamine neurons in the substantia nigra to treat Parkinson's disease. This nanosystem (ATB NPs) consists of gold nanoshell, an antibody against the heat-sensitive transient receptor potential vanilloid family member 1 (TRPV1), and β-synuclein (β-syn) peptides with a near infrared–responsive linker. ATB NPs by stereotactic injection target dopamine neurons expressing TRPV1 receptors in the substantia nigra. Upon pulsed near-infrared irradiation, ATB NPs, serving as nanoantennae, convert the light into heat, leading to calcium ion influx, depolarization, and action potentials in dopamine neurons through TRPV1 receptors. Simultaneously, β-synuclein peptides released from ATB NPs cooperate with chaperone-mediated autophagy initiated by heat shock protein, HSC70, to effectively eliminate α-synuclein fibrils in neurons. These orchestrated actions restored pathological dopamine neurons and locomotor behaviors of Parkinson's disease.

INTRODUCTION

Parkinson's disease (PD) is a chronic neurodegenerative disorder characterized by motor dysfunction and memory impairment, which result from the degeneration of dopamine (DA) neurons and the subsequent loss of DA loss in the substantia nigra (SN) pars compacta and striatum (*1*). The primary focus of the current medical therapies is to increase striatal DA levels, thereby alleviating symptoms in patients with PD. At present, the main therapeutic strategy for PD primarily lies in agents that increase DA signaling, notably L-dopa and DA agonists (*2*, *3*). Despite numerous studies, the progression of PD is seldom effectively remedied by the existing approaches due to their failure to restore degenerated neurons in the SN with precise spatial modulation, underscoring the urgent need for the development of innovative therapeutic strategies (*4*).

Deep brain stimulation (DBS) can rescue injured neurons by precisely exciting specific neurons using external stimuli such as light, electricity, sound, and magnetism (*5*). Among these stimuli, near-infrared (NIR) light stimulation has proven particularly effective in penetrating deep brain tissues, including the SN (*6*–*8*), depolarizing cells or inducing action potentials in neurons (*9*, *10*). Notably, these stimulus-mediated DBS often requires the permanent implantation of conduits. To overcome this limitation, an alternative approach is to use optogenetics, which selectively introduces exogenous genes coding for light-sensitive proteins (such as channelrhodopsins) into targeted neurons to modulate neuronal depolarization upon exposure to light stimuli (*11*, *12*). This technique is often accomplished with the use of transfection or viral transduction to drive light-sensitive gene expression, which raises safety issues. For example, cerebellar syndrome was reported in primates treated with viral vectors (*13*). Therefore, direct stimulation of endogenously expressed receptors in the damaged neurons in the SN without genetic modification would bypass above concerns. One such receptor is the heat-sensitive transient receptor potential vanilloid family member 1 (TRPV1), also an ion channel, which is highly expressed in DA neurons in the SN (*14*–*16*). These receptors can be activated by external heat stimulation to cause cation influx (*17*, *18*), a subsequent depolarization of neurons (*19*–*22*), and possibly the release of DA (*23*). Thus, we hypothesized that TRPV1 ion channels may serve as a modulatory target to activate DA neurons in the SN for PD therapy.

Prior studies have demonstrated that the degeneration and death of DA neurons in PD are primarily attributed to the deposition of α-synuclein (α-syn) fibrils, which form aggregates in the SN (*1*, *24*, *25*). Clearing these aggregates is a promising strategy for treating PD. The current approaches are mainly based on monoclonal antibodies with high affinity to α-syn fibrils (*26*); however, none of these drugs has successfully completed clinical trials. Therefore, there is a need for new treatments to restore DA neuron activity. Nanoparticles (NPs), such as graphene quantum dots and fullerenols, have been used to deconstruct aggregates via the charge interaction between NPs and α-syn fibrils (*27*–*29*), although this type of binding lacks specificity. In addition, an important factor contributing to the failure to clear α-syn aggregates is the disruption of the autophagic system by the accumulation of α-syn fibrils, leading to reduced levels of lysosomal enzymes or autophagic machinery (*30*, *31*). Restarting the intracellular autophagic process, such as the chaperone-mediated autophagy (CMA) pathway, is necessary for clearing pathologic α-syn. Therefore, an ideal therapeutic system for reducing the accumulation of neuronal α-syn aggregates, which has been a great challenge, would simultaneously disaggregate α-syn fibrils and initiate the autophagic process.

Here, we designed a photothermal, wireless DBS nanosystem, termed Au@TRPV1@β-syn (ATB) NPs. It comprises three components: (i) gold nanoshells (AuNSs) for NIR light-to-heat conversion (*32*–*35*), (ii) TRPV1 antibodies conjugated to AuNSs for specific targeting and activation of DA neurons, and (iii) β-synuclein (β-syn) peptides with a NIR-responsive linker for disaggregating α-syn

[1]New Cornerstone Science Laboratory, CAS Key Laboratory for Biomedical Effects of Nanomaterials and Nanosafety & CAS Center for Excellence in Nanoscience, National Center for Nanoscience and Technology of China, Beijing 100190, China. [2]Sino-Danish College, Sino-Danish Center for Education and Research, University of Chinese Academy of Sciences, Beijing 100049, China. [3]University of Chinese Academy of Sciences, Beijing 100049, China.
*Corresponding author. Email: cuixj@nanoctr.cn (X.C.); chenchy@nanoctr.cn (C.C.)

fibrils through specific binding to the α-syn nonamyloid–β component hydrophobic domain. After entry into the SN by a single stereotaxic injection, ATB NPs anchored to DA neurons through the TRPV1 receptor. Upon pulsed NIR irradiation (808 nm), the ATB NPs, acting as nanoantennae, sensed and converted the light into heat, which effectively restored degenerated DA neurons by activating the heat-sensitive TRPV1 receptor, leading to elevated Ca^{2+} influx and action potentials. Concurrently, the NPs eliminated α-syn aggregates and reduced pathological α-syn fibrils by releasing β-syn peptides and stimulating the CMA process. ATB NPs ultimately induced increased DA levels in the striatum and reversed locomotor behavior in α-syn preformed fibril (PFF)–induced PD mice. This "wireless" DBS therapeutic approach may open new avenues in the treatment of PD and other neurodegenerative diseases.

RESULTS AND DISCUSSION

ATB NPs activate and depolarize the TRPV1-positive cells under NIR irradiation

First, we fabricated multifunctional ATB NPs that can achieve wireless photothermal DBS in the SN after NIR irradiation, with three modules (Fig. 1A): (i) heat transfer module: AuNSs (with SiO_2 core) sensitivity to NIR irradiation leads to the generation of mild heat due to surface plasmon resonance; (ii) targeting and activating module: conjugation with a specific TRPV1 antibody raised against the extracellular loop of TRPV1 (400 to 500 amino acids, containing the extracellular epitope 455 to 468 amino acids) for delivery into TRPV1-positive ($TRPV1^+$) cell types in the SN; (iii) degrading module: linkage to a borate ester [NIR-responsive linker (*36*, *37*)] containing β-syn peptides [36 to 45 amino acids, all D type, RTKSGVYLVG (*38*); Fig. 1B], which will release the β-syn peptides into cells after NIR stimulation and disaggregate α-syn fibrils. We initially prepared and characterized the borate ester ligands formed between mercaptophenylboric acid (MPBA) and β-syn peptides (fig. S1, A to C). The Fourier transform infrared (FTIR) spectroscopy bands at 1417, 1365, and 1026 cm^{-1} indicate the presence of B—O bonds and borates (fig. S1A). The nuclear magnetic resonance (NMR) spectra in fig. S1B show a downfield shift of the protons on the benzene unit of MPBA after reacting with β-syn peptides to form boronic esters. This was due to the stronger electron-withdrawing property of the phenylboronate ester, leading to a decline of cloud density on the benzene unit. Consequently, the downfield shift of the protons occurs. The ^{11}B NMR spectra in fig. S1C further demonstrate the transformation of boron from trihedral to tetrahedral, confirming the formation of a boronic ester. After TRPV1 and MPBA–β-syn peptide ligands were attached to the AuNSs, FTIR spectra indicated the presence of an amido bond (1656 cm^{-1}; amide bands appeared after AuNSs were modified with the TRPV1 antibody) and B—O bonds (1417, 1365, and 1026 cm^{-1}; Fig. 1C). The diameter changes from ~166 nm for AuNSs to ~207 nm for ATB NPs indicate the conjugation of TRPV1 and β-syn to the NPs, as visualized by dynamic light scattering and transmission electron microscopy (TEM) (fig. S1, D and E). Moreover, a red shift in the maximum ultraviolet (UV) adsorption suggests the successful addition of ligands into the AuNSs (fig. S1F). To evaluate the ability of ATB NPs to respond to pulse NIR irradiation, we irradiated the NP suspensions with an 808-nm laser. ATB NPs showed excellent photothermal conversion performance under various laser powers and frequencies, even at low particle concentrations (fig. S1, G to I). Furthermore, the size of the NPs decreased (fig. S1J) and the infrared peak from the B—O bond reappeared after laser irradiation (fig. S1K), suggesting that β-syn peptides were released from ATB NPs due to the broken boronic ester caused after NIR irradiation. Overall, the fabricated ATB NPs enabled the generation of mild heat and release of β-syn peptides under the 808-nm NIR irradiation.

We next investigated the ability of ATB NPs to target to the cell membrane of DA neurons. We first confirmed the presence of TRPV1 in isolated primary dopaminergic neurons (cultured for 7 days). The colocalization of TRPV1 with tyrosine hydroxylase (TH; DA neuron marker) indicated that mature DA neurons express endogenous TRPV1 receptors (fig. S2A, top), as well as other mature neuronal markers, including class III β-tubulin (TuJ1), microtubule-associated protein 2 (MAP2), and vesicular monoamine transporter 2 (VMAT2; fig. S2A, middle and bottom). After incubation with primary DA neurons for 24 hours, ATB NPs did not induce cytotoxicity in DA neurons, even at the high concentration of 5×10^9 particles/ml (fig. S2B), suggesting an excellent biocompatibility of ATB NPs. We chose a concentration of 1×10^9 particles/ml for all subsequent cellular experiments. After incubation for 24 hours, ATB NPs were mainly located in the cell membrane of DA neurons (Fig. 1D, left). To verify that the highly expressed TRPV1 receptors on DA neurons mediate the anchoring of ATB NPs to the cell membrane, we transfected human embryonic kidney (HEK) 293T cells with a TRPV1 expression plasmid and incubated the cells with ATB NPs (1×10^9/ml) for 24 hours. As expected, ATB NPs were present in the cytoplasm in TRPV1-negative ($TRPV1^-$) cells, while $TRPV1^+$ cells exhibited the most NPs around the cell membrane (Fig. 1D, right). We further visualized this TRPV1-mediated docking effect on the cell membrane in α-syn PFF-induced degenerated DA neurons. After incubation with AuNSs or Au@TRPV1 NPs (AT NPs) for 24 hours, the AT NPs mainly localized to the cell membrane (fig. S2C). In contrast, most of the AuNSs, without TRPV1 antibody modification, were internalized by neurons. To further confirm the role of TRPV1 in ATB NPs binding to cell membranes, we blocked the TRPV1 channel with a specific TRPV1 antibody for 3 hours. Following a 24-hour incubation with ATB NPs, cells were observed using laser reflection technology of confocal laser scanning microscopy. In the absence of TRPV1 receptor, most ATB NPs were found in neuronal cells and axons (white arrows; fig. S2D). These data suggest that ATB NPs target the cell membranes of DA neurons through the TRPV1 receptors.

We proceeded to explore whether ATB NPs and pulsed NIR stimuli can activate primary DA neurons in the presence of ATB NPs, using Ca^{2+} influx as an indicator of TRPV1 activity (Fig. 1E). Our results show that Ca^{2+} influx only increased when both ATB NPs and NIR laser (2 W, 20 ms per pulse, 20 Hz, 1 min) were applied to PFF-treated DA neurons, as manifested by a continuous enhancement of the fluorescence intensity of Fluo-4 AM (Fig. 1F, right, and movies S1 to S3). The intracellular Ca^{2+} concentration in PFF-treated neurons remained unchanged in the absence of either the ATB NPs or external laser stimulation (Fig. 1F), indicating that ATB NPs only trigger Ca^{2+} influx under NIR laser stimulation. To confirm that the Ca^{2+} influx was mediated by TRPV1, we again transfected HEK-293T cells with a TRPV1 expression plasmid. Similarly, we found that ATB NPs and NIR laser stimulation promoted Ca^{2+} influx only in $TRPV1^+$ cells but not in $TRPV1^-$ cells (Fig. 1G and movies S4 to S6). Thus, ATB NPs elicited Ca^{2+} influx under NIR laser stimulation through TRPV1. Consistent with the results from Ca^{2+} influx, we also observed that the ATB NPs induced inward currents in $TRPV1^+$

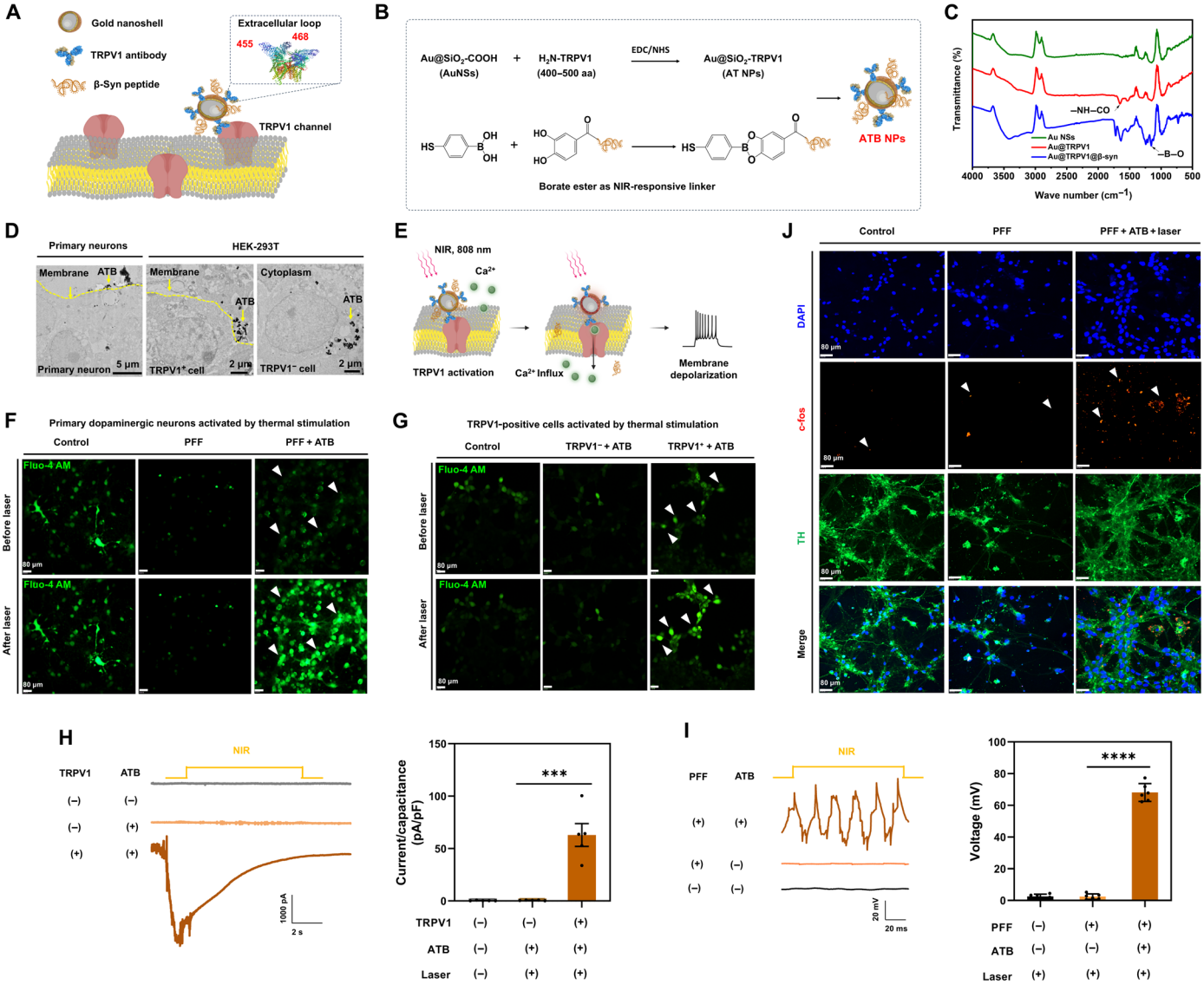

Fig. 1. ATB NP–mediated photothermal stimulation promotes the activation and depolarization of TRPV1$^+$ cells in vitro. (**A** and **B**) An illustration of the design of ATB NPs. ATB NPs were synthesized by conjugating the TRPV1 antibody against the TRPV1 extracellular domain [400 to 500 amino acids (aa)] and β-syn peptides to AuNSs. (**C**) Representative FTIR spectra of AuNSs, AT NPs, and ATB NPs. (**D**) Distribution of ATB NPs (1×10^9/ml) in primary dopaminergic neurons and HEK-293T cells transfected with or without TRPV1 plasmid, as shown by TEM. (**E**) Working model of ATB NP–mediated photothermal stimulation activating TRPV1 and Ca^{2+} influx in cells, as determined by Fluo-4 AM probe. (**F**) Representative Ca^{2+} influx of control, PFF neurons, and PFF neurons treated with ATB NPs (1×10^9/ml) for 24 hours, before and after NIR laser irradiation (2 W, 20 ms per pulse, 20 Hz) for 1 min. Scale bars, 80 μm. (**G**) Ca^{2+} influx of HEK-293T cells transfected with TRPV1 plasmid or empty vector (set as control) incubated with ATB NPs, before and after NIR laser irradiation. Scale bars, 80 μm. (**H**) Whole-cell patch-clamp traces of TRPV1$^+$ or TRPV1$^-$ cells in the presence or absence of ATB NPs for 24 hours and NIR laser treatment for 1 min ($n = 5$, five replicates). (**I**) Action potentials in PFF-treated DA neurons in response to ATB NPs and NIR laser irradiation ($n = 6$, six replicates). (**J**) Representative immunofluorescence images of c-fos in primary dopaminergic neurons treated with PFF (2 μg/ml) for 3 days, followed by ATB NPs incubation for 24 hours and NIR laser irradiation for 1 min. Scale bars, 80 μm. The data are expressed as the means ± SD. Statistical significance was tested using a two-tailed *t* test and one-way analysis of variance (ANOVA) analysis. ***$P < 0.001$ and ****$P < 0.0001$. (A), (B), and (E) created using BioRender.com.

cells but not in TRPV1$^-$ cells under NIR laser stimulation, as determined by electrophysiological, whole-cell patch-clamp experiments (Fig. 1H). As a result, ATB NPs and NIR laser stimulation induced depolarization in PFF-treated DA neurons, compared to the neurons without ATB NP treatment (Fig. 1I), thus facilitating their greater action potentials and activation. Next, we assessed the impact of ATB NPs and NIR laser stimulation on the activation of α-syn PFF-treated DA neurons, using the immediate early protein, c-fos, as an indicator of activity in electroactive neurons. ATB NPs and NIR stimulation elevated the proportion of c-fos–positive cells in PFF-treated neurons compared to untreated controls and PFF only–treated neurons (Fig. 1J). These results provide compelling evidence for the indispensability of three key components, ATB NPs, NIR laser, and TRPV1, in the activation of neurons through photothermal stimulation. Specifically, the ATB NPs activated neurons under NIR laser irradiation by acting on the TRPV1 receptor.

ATB NP–mediated photothermal stimulation promotes disaggregation of α-syn PFF in vitro

Since the formation and aggregation of α-syn fibrils in DA neurons have been suggested to be the primary cause of neuronal inactivation and death in PD (*1*, *24*, *25*), promoting the degradation of α-syn fibrils in neurons is a potential therapeutic strategy. To explore this, we examined the inhibitory effect of β-syn peptides on α-syn fibrillization (Fig. 2A). The results of thioflavin T (ThT; see working principle in Materials and Methods) fluorescence show that, in the absence of β-syn peptides, α-syn monomers gradually form fibrils (0 to 168 hours; Fig. 2B, purple), while the addition of β-syn peptides interrupted this process (Fig. 2B, orange). In addition, blue native polyacrylamide gel electrophoresis (BN-PAGE) analysis revealed that in combination with β-syn peptides, α-syn monomers behave similarly to α-syn monomers alone (Fig. 2C, lower separation gel); no α-syn fibril band was present in the loading well, which is consistent with previous findings (*38*). These results indicate the inhibitory effect of β-syn peptides on the formation of α-syn fibrils. We further examined the effect of β-syn peptides on the disaggregation of α-syn PFF (Fig. 2D). The β-syn peptides markedly dissociated α-syn PFF into fragments or monomers (Fig. 2E, blue), which was concurrent with the gradual appearance of α-syn monomers at 24 to 168 hours in the lower separation gel (Fig. 2F). The breakdown of the fibrils was further evidenced by morphological changes in α-syn PFF and α-syn monomers with the addition of β-syn peptides (Fig. 2G). Meanwhile, we observed similar effects of β-syn peptides on human-derived α-syn (fig. S3, A to C). To be noticed, there was no obvious disaggregation of α-syn fibrils under 43°C for 7 days, suggesting that heat alone triggered by NIR laser irradiation did not induce α-syn fibril disaggregation (fig. S4). The above results demonstrate that β-syn peptides can inhibit both the formation and promote the disaggregation of α-syn fibrils. A possible mechanism for this might be the presence of aromatic tyrosine amino acids in β-syn peptide, which provide a hydrophobic binding interface with α-syn, resulting in a strong affinity binding with an affinity constant of 1 μM, thus increasing the binding ability of β-syn peptides in the cytoplasm (*38*). The binding affinity between the α-syn monomers was 43.78 ± 9.70 μM (fig. S5), markedly lower than that of β-syn peptides binding to α-syn monomers. Therefore, the interactions between α-syn monomers are weaker than that of β-syn peptides and α-syn monomer. To further investigate how the β-syn peptides disaggregate the α-syn fibrils, we used isothermal titration calorimetry (ITC) to study the interaction between β-syn peptides and α-syn fibrils. There was a strong interaction between β-syn peptides and α-syn fibrils, with a dissociation constant (K_d) value as 0.386 μM (Fig. 2, H and I). Thermodynamic analysis (Fig. 2J) revealed that the binding is driven by a combination of hydrophobic and electrostatic interactions, indicated by a positive entropy change ($\Delta S > 0$) and a negative enthalpy ($\Delta H < 0$) (*39*, *40*). In general, aromatic amino acids are crucial in accelerating amyloid fibril formation (*41*). The Tyr amino acids present in the β-syn peptides may form π-π stacking with the aromatic residues in the fibrils (*38*), thus disrupting the β sheet structure's stability (*42*). Subsequent electrostatic interactions further facilitate the fibril disaggregation (*27*, *28*).

Given that β-syn peptides can disaggregate α-syn fibrils, we next applied this strategy to primary DA neurons. α-Syn PFF elicited elevated expression and accumulation of phosphorylated α-syn (p–α-syn) at Ser^{129} (pα-synSer^{129}) in mature DA neurons after PFF treatment for 3 days (Fig. 2K, middle). This highly toxic event led to the degeneration of DA neurons, including decreased expression of TH (rate-limiting enzyme in DA synthesis). In contrast, when ATB NPs were added to the neurons and stimulated by a pulsed NIR laser, the released β-syn peptides are likely to enter cells through passive diffusion, as does the α-syn monomer due to the high homology between α-syn and β-syn, particularly in the N-terminal region (*43*, *44*). Therefore, the aggregation of α-syn PFF was alleviated and the expression of TH was restored in neurons (Fig. 2K, bottom, and fig. S6). These findings were further corroborated by Western blot analysis, which demonstrated that only PFF-treated DA neurons exhibited increased levels of p–α-syn in the SDS-insoluble fraction, whereas ATB NPs, combined with pulsed NIR laser excitation, showed decreased expression (Fig. 2L). Notably, α-syn PFF treatment also caused the disruption in the neuronal network, as indicated by a decrease in the neuronal connections and a loss in the neuronal markers, TuJ1 and MAP2, by immunostaining (Fig. 2M). However, the addition of ATB NPs with NIR irradiation led to a reconstruction of the network between neurons, with increased expression of TuJ1, VMAT2, and DA transporter (DAT; Fig. 2N, left). A plausible explanation for this is that the deposition of harmful fibrils in neurons was diminished by ATB NP–transduced thermal therapy after NIR irradiation, thus remodeling the connections and morphology of neurons.

Both NIR stimuli and nanomaterial-induced activation may contribute to the restoration of diseased neurons by promoting neurogenesis and outgrowth at the cellular level (*45*–*48*). Therefore, we further elucidated the mechanism of ATB NP restoration of neuronal function. We found that the ATB NPs activated HSC70 (an important molecular heat shock protein chaperone) and lysosomal-associated membrane protein 2A (LAMP2A) under NIR stimulation (Fig. 2N, right), which promoted the degradation of α-syn PFF through the chaperone-mediated autophagy process. NPs have been used as general chaperone-mediated autophagy activators (*49*). For instance, on the basis of the characteristics of chaperone activation by heat, NPs can serve as thermal transducers to stimulate the increased transcription and expression of heat shock protein genes (*33*, *50*), which recognize and bind to the C-terminal motif, an autophagy recognition site (VKKDQ), of α-syn and then transport it to the lysosome for degradation via LAMP2A (*51*–*53*), thus restoring neurons and their expression of TH (Fig. 2N, right). Notably, the NIR-induced mild heat generation promoted the specificity of the CMA process. In particular, cell viability assays provided conclusive evidence that ATB NPs successfully counteracted the α-syn PFF-induced death of DA neurons (fig. S7). Treatment with ATB NPs resulted in a complete elimination of neuron death, reducing it from 68% in PFF-treated cells to zero in ATB NP–treated neurons. Together, these findings suggest that ATB NPs can restore the function and viability of DA neurons by accelerating the disaggregation and clearance of α-syn PFF under NIR stimuli in vitro.

ATB NP–mediated wireless DBS induces the activation of DA neurons and DA release in mice

After determining in vitro that ATB NPs with NIR irradiation can restore the function and viability of DA neurons, we next tested the capability of the treatment to protect against neuronal degeneration in an α-syn PFF-induced PD mouse model. We first verified the expression of TRPV1 in the SN before performing experiments with ATB NPs. Coronal sections of the mouse brain showed an overlap of

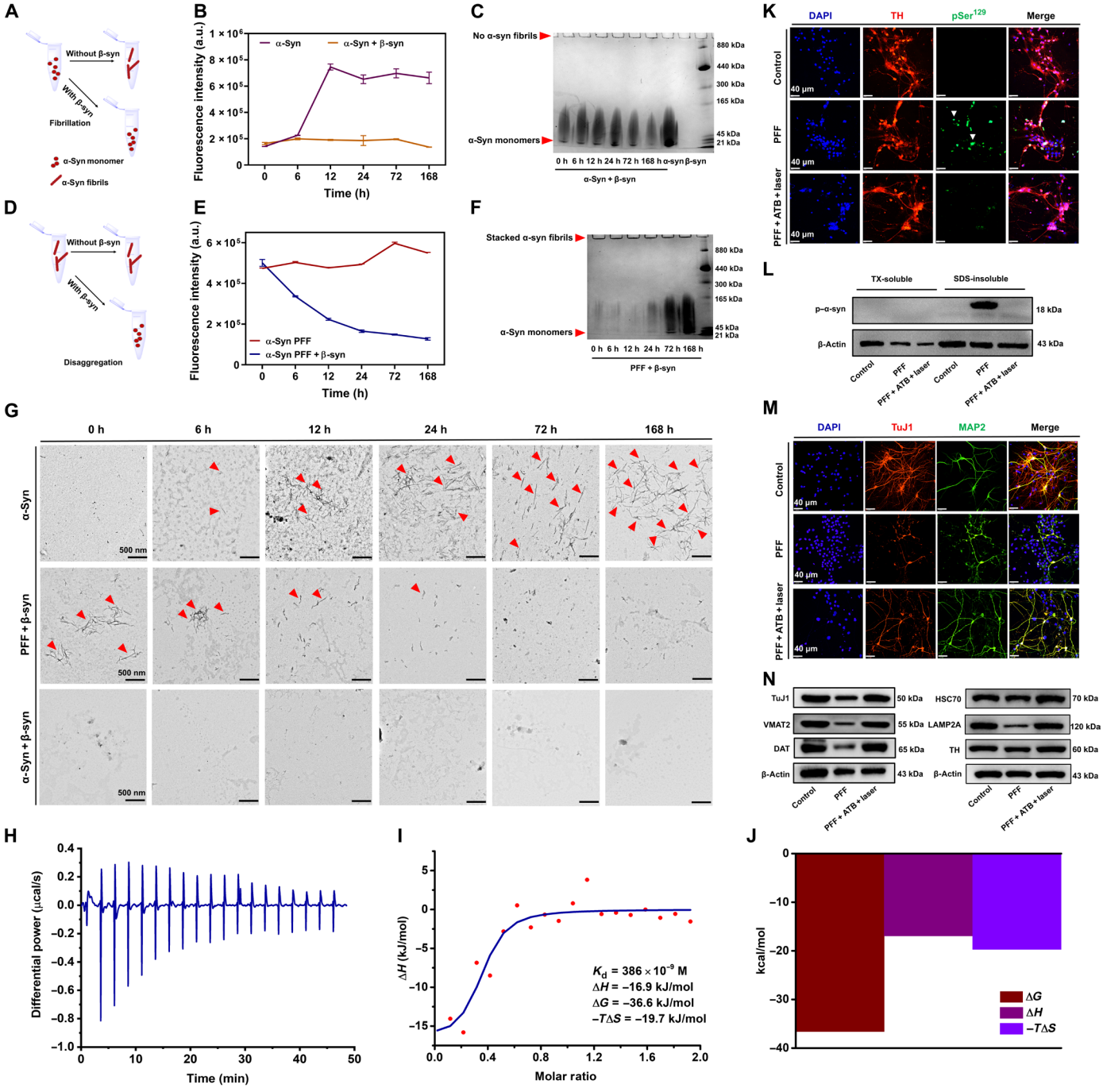

Fig. 2. ATB NP–mediated photothermal stimulation promotes disaggregation of α-syn PFF in vitro. (**A**) Schematic illustration of α-syn fibrillization (α-syn monomer, 2 mg/ml) in the presence and absence of β-syn peptides (5 mg/ml). (**B**) α-Syn monomer fibrillization in the presence and absence of β-syn peptides by ThT fluorescence ($n = 3$, three replicates). a.u., arbitrary units; h, hours. (**C**) BN-PAGE analysis of α-syn fibrillization in the presence or absence of β-syn peptides at indicated time points (0 to 168 hours). (**D**) Schematic illustration of α-syn PFF disaggregation (α-syn monomer, 2 mg/ml) in the presence and absence of β-syn peptides. (**E**) α-Syn PFF disaggregation in the presence and absence of β-syn peptides ($n = 3$, three replicates). (**F**) BN-PAGE images showing α-syn PFF disaggregation induced by β-syn peptides at the indicated time points (0 to 168 hours). (**G**) Representative TEM images of α-syn monomers or PFF at indicated time points (0 to 168 hours) in the presence and absence of β-syn peptides. Scale bars, 500 nm. (**H** to **J**) The interaction between β-syn peptides and α-syn fibrils, as determined by ITC and thermodynamic analysis. (**K**) Representative confocal images of p–α-syn in mature neurons treated with PFF (2 μg/ml) and ATB NPs (1×10^9/ml) and NIR laser (2 W, 20 ms per pulse, 1 min). Scale bars, 40 μm. (**L**) Expression of p–α-syn from the detergent soluble and insoluble fractions from mature neurons treated with ATB NPs and NIR laser, as determined by Western blot. TX, Triton X-100. (**M**) Representative confocal images of neural morphology in the presence of ATB NPs and NIR laser. Scale bars, 40 μm. (**N**) Expression of TuJ1, VMAT2, DAT, TH, HSC70, and LAMP2A in mature neurons treated with ATB NPs and NIR laser. All experiments were repeated at least three times. The data are expressed as the means ± SD.

TRPV1 with TH-positive neurons (Fig. 3A), indicating the presence of this receptor in the DA neurons. After delivery of ATB NPs into SN, no change in the expression of the TRPV1 receptor was observed (Fig. 3A). Next, over the course of 3 months, we unilaterally injected α-syn PFF (5 μg/2 μl) into the striatum of healthy mice to induce parkinsonian disease, followed by injection of ATB NPs (1×10^{11}/ml) into the SN (Fig. 3B). The injected ATB NPs mainly localized and stably resided in the SN region of the brain for at least 5 weeks, rarely spreading to other regions, such as the hippocampus and cortex, as determined by laser ablation inductively coupled plasma mass spectrometry (LA-ICP-MS; P element was used to visualize the structure of the mouse brain) and ICP-MS (Fig. 3, C and D). We

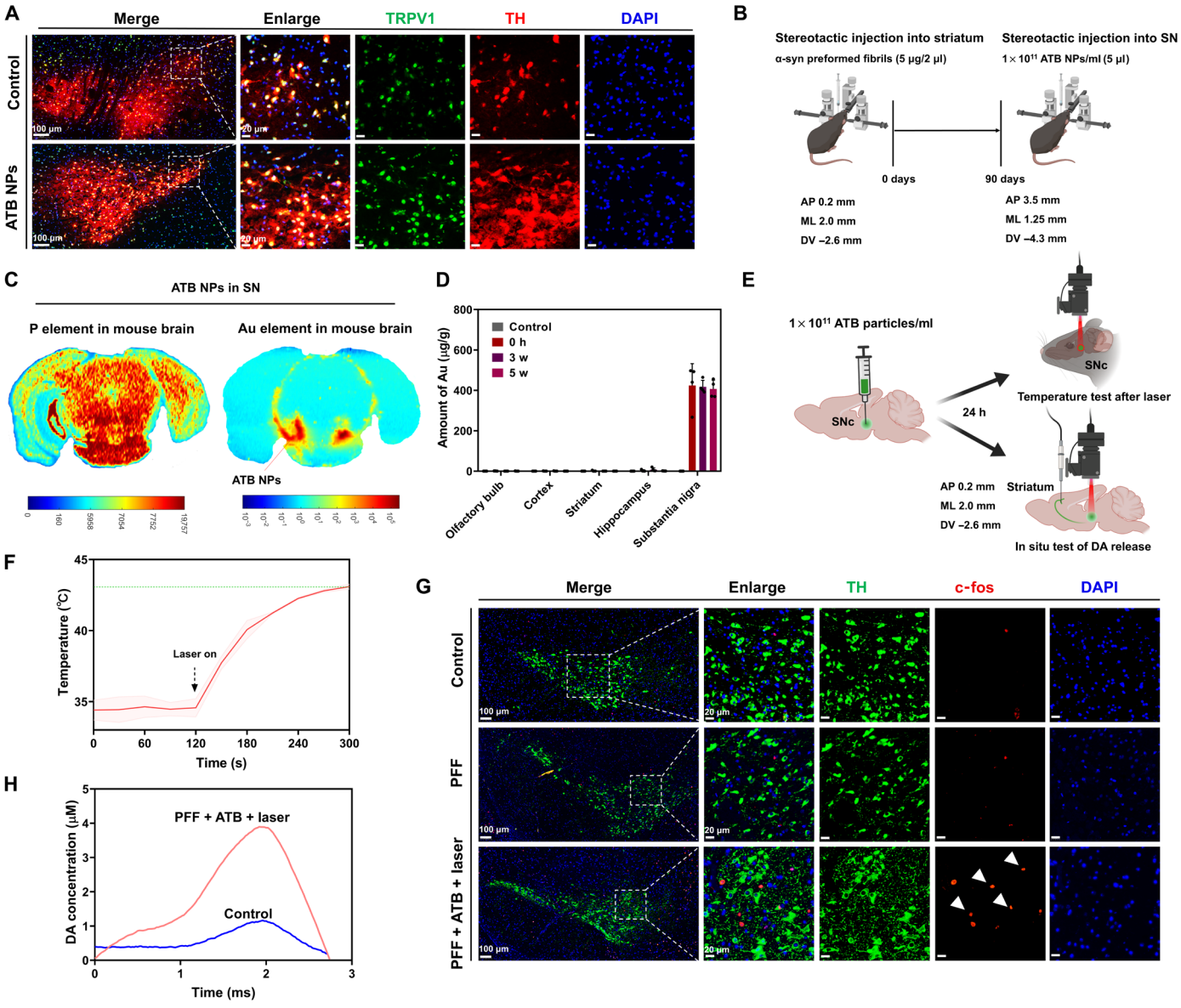

Fig. 3. ATB NPs in the SN induce the activation of DA neurons and DA release in mice. (**A**) Representative immunofluorescence images showing TRPV1 expression in the TH-positive cells of SN in control and ATB-treated mice. ATB NP injection did not affect the TRPV1 expression in the mice. (**B**) Schematic representation of the treatment of C57BL/6J mice after stereotactic injection of PFF (5 μg) in the striatum for 3 months and subsequent ATB NPs (1×10^{11}/ml, 5 μl) injection into the SN at different injection coordinates. (**C**) Distribution of ATB NPs in the brain, as determined by LA-ICP-MS after injection. Au appears in the SN zone. (**D**) Quantitative measurement of Au in the olfactory bulb, cortex, striatum, hippocampus, and SN in mice. The ATB NPs were stereotactically injected into the SN, and the content of Au in different regions of the mouse brain was measured at the indicated time points [0 to 5 weeks (w)] by ICP-MS ($n = 4$, biologically independent mice). (**E**) Schematic illustration of ATB NP injection into the SN 1 day before NIR irradiation and DA release measurement. SNc, substantia nigra pars compacta. (**F**) Temperature changes in the mouse brain, as recorded by thermal camera, after NIR irradiation for 3 min. (**G**) Representative confocal images showing the expression of c-fos in the SN of control, PFF mice, and PFF mice treated with ATB NPs and NIR laser. (**H**) Transient DA release in the striatum in response to ATB NPs and NIR stimulation in control and PFF-treated mice. A carbon fiber electrode was implanted into the striatum to monitor the DA levels in the striatum in real time using FSCV. All experiments were repeated at least three times. The data are expressed as the means ± SD. (B) and (E) created using BioRender.com.

then placed an optic fiber 1 cm above the skull surface of the mice to measure the temperature after exposure to pulsed NIR laser excitation (Fig. 3E). The thermal probe shows that the heat created by the nanosystem was sufficient to reach the threshold temperature 43°C to trigger TRPV1 channels within 3 min in the mice (Fig. 3F). The NIR-induced DA neuron activation was also evidenced by increased expression of c-fos, only in PFF-treated mice where neurons were excited by NIR irradiation in the presence of ATB NPs (Fig. 3G, white arrowheads). Since the DA neurons in the SN transport DA to the striatum through a nigrostriatal dopaminergic pathway to participate in motor regulation, we investigated whether the evoked neuronal activity could enhance DA release in the striatum, using fast-scan cyclic voltammetry (FSCV). The SN of anaesthetized PFF-treated mice was first injected with ATB NPs, after which a carbon fiber electrode was stereotactically implanted into the striatum. We then administered NIR stimulation and monitored the changes in DA levels in the striatum in real time (control: no treatment). Upon NIR irradiation, DA release was markedly increased in the ATB NP–treated mice, compared to control (Fig. 3H). Together, these results suggest that ATB NPs plus NIR irradiation can increase DA neuronal activity in the SN, including DA release in the striatum of mice.

ATB NP–mediated wireless photothermal DBS alleviates symptoms of PD in mice

We proceeded to examine whether ATB NP–mediated wireless DBS can alleviate the symptoms of PFF-induced PD mice, by stereotactically injecting a single bolus of ATB NPs into the SN [phosphate-buffered saline (PBS) treatment was used as a control) and applying pulsed NIR irradiation once every 7 days for a total five treatments (Fig. 4A). After the therapy, we conducted rotarod and pole tests to evaluate locomotor activity. As expected, we observed a decreased in latency to fall in the rotarod test and an increased time taken to climb down the pole in the PFF-injected mice compared the control group (Fig. 4, B and C), indicating a decreased grip strength due to the loss of TH-positive DA neurons. However, treatment with the ATB NPs plus NIR irradiation remarkably ameliorated the motor deficits elicited by PFF treatment. In addition to the rotarod and pole tests, we also conducted open field tests to assess locomotor activity and exploratory behavior. The PFF-injected mice exhibited reduced travel paths and total distances in the open field and center square (Fig. 4, D and E), as well as decreased average velocity and entries into the center zone (Fig. 4, F to H), compared to the control group. In contrast, PFF mice treated with ATB NPs and NIR irradiation performed similarly to controls, indicating notably motor behavior recovery in PFF mice from the ATB NP–mediated wireless DBS therapy.

We next investigated how the ATB NP–mediated wireless DBS therapy alleviated the symptoms of PFF-induced PD mice. By visualizing the DA neurons, we found a substantial loss of TH-positive cells in the SN and striatum in PFF-treated mice (Fig. 5A, top and middle), indicating a reduction in DA neurons, compared to control. However, this loss was reversed when we used the ATB NP plus NIR irradiation treatment to the PFF mice. Apart from the number of neurons, PFF-induced toxicity also negatively affected the morphology of DA neurons, resulting in fewer Nissl-positive cells with clumped shapes in the SN of the PFF mice (Fig. 5A, bottom). In contrast, ATB NP plus NIR irradiation markedly restored the number of Nissl-positive neurons. The dysfunctional neuronal network caused by PFF injection was reconstructed by this therapy, as revealed by the increased expression of cytoskeleton-associated proteins, TuJ1 and MAP2 (Fig. 5B). Thus, a remodeling of the signal transduction and communication between neurons was achieved.

The aggregation of α-syn fibrils in the SN is recognized as a causative factor in the pathology of PD, playing a pivotal role in the dysfunction and eventual death of DA neurons. To evaluate the impact of ATB NP–mediated wireless DBS therapy on α-syn PFF pathology, we injected PFF into the striatum of mice for a duration of 3 months and observed its localization. We found the spread of PFF from the striatum to around the cortex and the hippocampus, as well as its deposition in the SN, through immunohistochemistry and immunofluorescence staining (Fig. 5, C and D). However, this spread and deposition were effectively prevented and cleared by the ATB NP–mediated wireless photothermal DBS, showing disappeared α-syn PFF pathology labeled by pα-synSer^{129} antibody (Fig. 5, C to E). In support of these results, Western blot analysis confirmed that the ATB NPs and NIR laser markedly decreased the levels of pα-syn in the SDS-insoluble fraction in the SN of the PFF mice compared to the untreated PFF-injected mice (Fig. 5F), indicating an effective targeting of α-syn fibrils by the ATB NP–mediated wireless photothermal DBS. We next explored whether the specific mechanism of this action in vivo mirrored our in vitro results (Fig. 2N). Administration of the photothermal DBS therapy activated the expression of the heat shock protein, HSC70, in the SN, leading to an increased expression of the lysosomal protein, LAMP2A, thus activating CMA to degrade insoluble PFF fibrils (Fig. 5G). Ultimately, this orchestrated series of actions resulted in the restoration of the number of TH-positive DA neurons and alleviated the PD symptoms caused by PFF (Fig. 5G).

In addition to the PFF-induced PD model, we also established an 1-methyl-4-phenyl-1,2,3,6-tetrahydropyridine (MPTP)–induced PD mouse model to assess the universality of the wireless photothermal DBS therapy. The treatment also promoted motor recovery of the MPTP mice (fig. S8, A to H). These changes were mainly attributed to the activation of neurons and microglia by the wireless photothermal DBS, which accordingly enhanced the CMA process to clear the pathological aggregates and prevent the loss of TH/Nissl neurons (fig. S9, A to D). Moreover, we explored the biocompatibility of the ATB NP–based treatment in mice. Biochemical indicators of toxicity in the serum of ATB NP–treated mice were similar to those of controls (table S1), indicating to apparent untoward effects of the treatment (fig. S10). Collectively, our findings indicate that ATB NP–mediated wireless DBS therapy is a viable concept worthy of additional consideration in the search for an effective PD remedy.

Last, we evaluated the safety of ATB NP–mediated wireless DBS therapy, especially the influence of temperature of 43°C induced by NIR laser to the DA neurons and other cells by flow cytometry. Obviously, laser treatment did not affect the viability of DA neurons (TH-positive), TRPV1$^+$ and TRPV1$^-$ cells (TRPV1 antibody–labeled), astrocytes [glial fibrillary acidic protein (GFAP)–positive], or microglia (CD11b-positive and CD45-intermediate) in the SN compared to control (fig. S11). This indicates that the heat generated by the ATB NPs and laser treatment did not cause any considerable damage to the DA neurons and TRPV1$^+$ cells. Similarly, terminal deoxynucleotidyl transferase–mediated deoxyuridine triphosphate nick end labeling staining revealed no obvious apoptosis in these cells and main brain areas (SN, hippocampus, midbrain, and cortex) of mice treated with NIR laser and ATB NPs (fig. S12, A and B), suggesting the good biocompatibility of this therapeutic system.

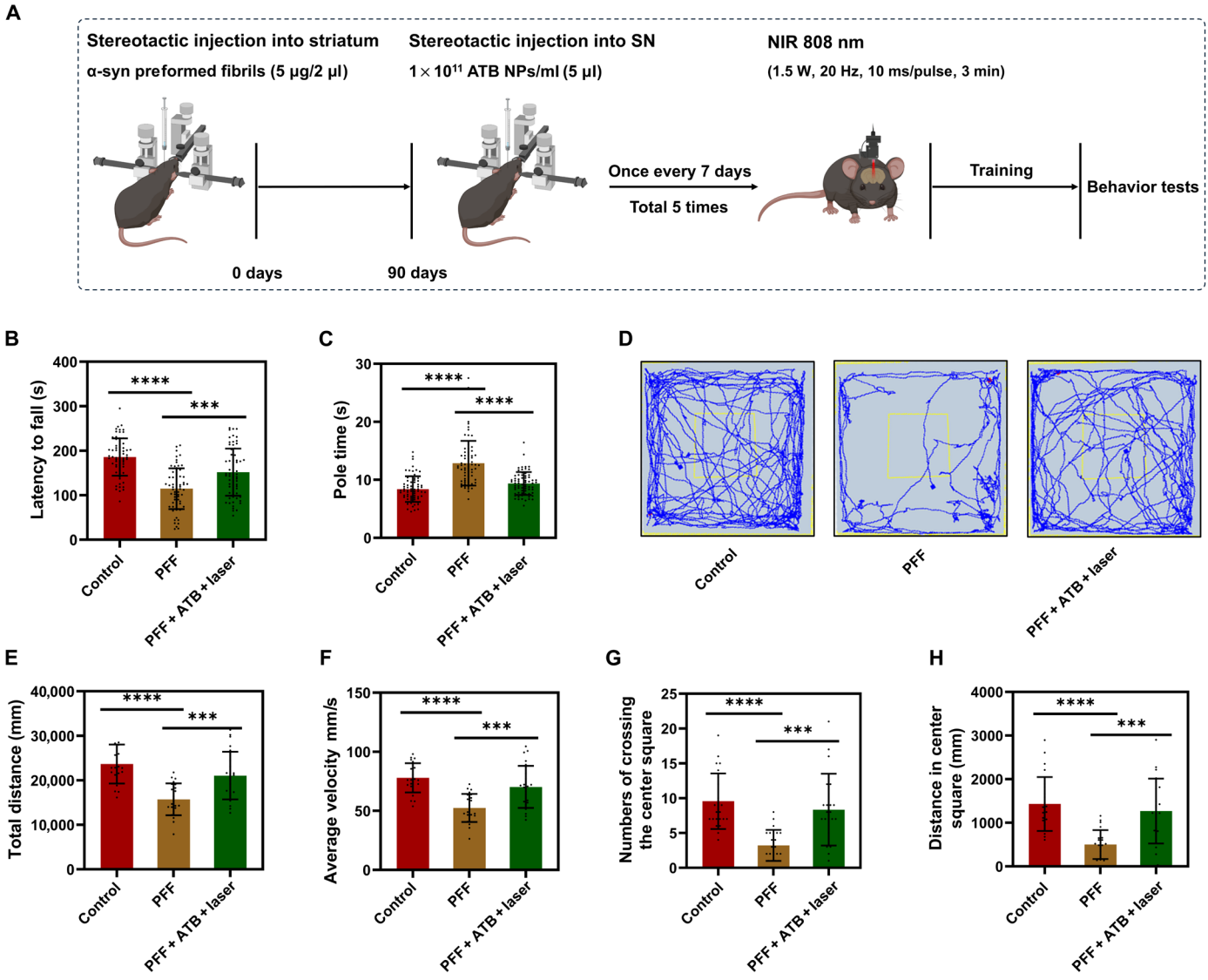

Fig. 4. ATB NP–mediated wireless photothermal DBS promotes motor recovery in PFF mice. (**A**) Schematic representation of the treatment of C57BL/6J mice after stereotactic injection of PFF (5 μg) in the striatum for 3 months and subsequent single injection of ATB NP (1×10^{11}/ml, 5 μl) into the SN and NIR laser application (1.5 W, 10 ms per pulse, 3 min) once every 7 days for a total five treatments. Created using BioRender.com. (**B**) Rotarod test assessment of control, PFF mice, and PFF mice treated with ATB NPs and NIR laser ($n = 69$, biologically independent mice). The data are expressed as the means ± SD. (**C**) Pole test assessment of control, PFF mice, and PFF mice treated with ATB NPs and NIR laser ($n = 69$, biologically independent mice). (**D**) Representative movement trails of control, PFF mice, and PFF mice treated with ATB NPs and NIR laser in the open field test. (**E** to **H**) Quantitative measurement of locomotion activity in the open field test of control, PFF mice, and PFF mice treated with ATB NPs and NIR laser. The data of total distance (E), average velocity in the whole field (F), entry numbers (G), and distance (H) in the center zone of the open field are shown ($n = 23$, biologically independent mice). The data are presented as the means ± SD. Statistical significance was tested using a two-tailed *t* test and one-way ANOVA analysis. ***$P < 0.001$; ****$P < 0.0001$. All animal experiments were repeated at least three times.

We also investigated the final fate and long-term effects of ATB NPs after stereotaxic injection in the SN for 8 weeks. ATB NPs were stably remained in the SN without considerable translocation to other tissues (heart, liver, spleen, lung, and kidney), feces, and fluids (blood and urine), with a few particles' translocation to cerebrospinal fluid at 8 weeks (fig. S13, A and B). Confocal laser reflectivity imaging displayed that ATB NPs (red) mainly localized around TH-positive DA neurons in the SN (white arrows; fig. S14A), confirming the sustained presence of ATB NPs in the SN for at least 8 weeks. Meanwhile, there was minor uptake of ATB NPs by microglia in the SN (white arrows; fig. S14B). To further examine the interaction of ATB NPs and nearby phagocytes, we isolated and cultured primary mesencephalic cells without 5-fluoro-2′-deoxyuridine to inhibit glial cell growth. After incubation with ATB NPs (1×10^9/ml) for 24 hours, we observed that a small number of NPs (yellow arrows) were internalized by microglia (Iba-1) and astrocytes (GFAP) (fig. S15, A and B). As microglia, the primary immune cells in the brain (*54*), are involved in NP clearance, this process may aid in the excretion of NPs into the brain tissue fluid. A recent study has shown that gold NPs (10 nm) injected intracerebrally have a brain clearance

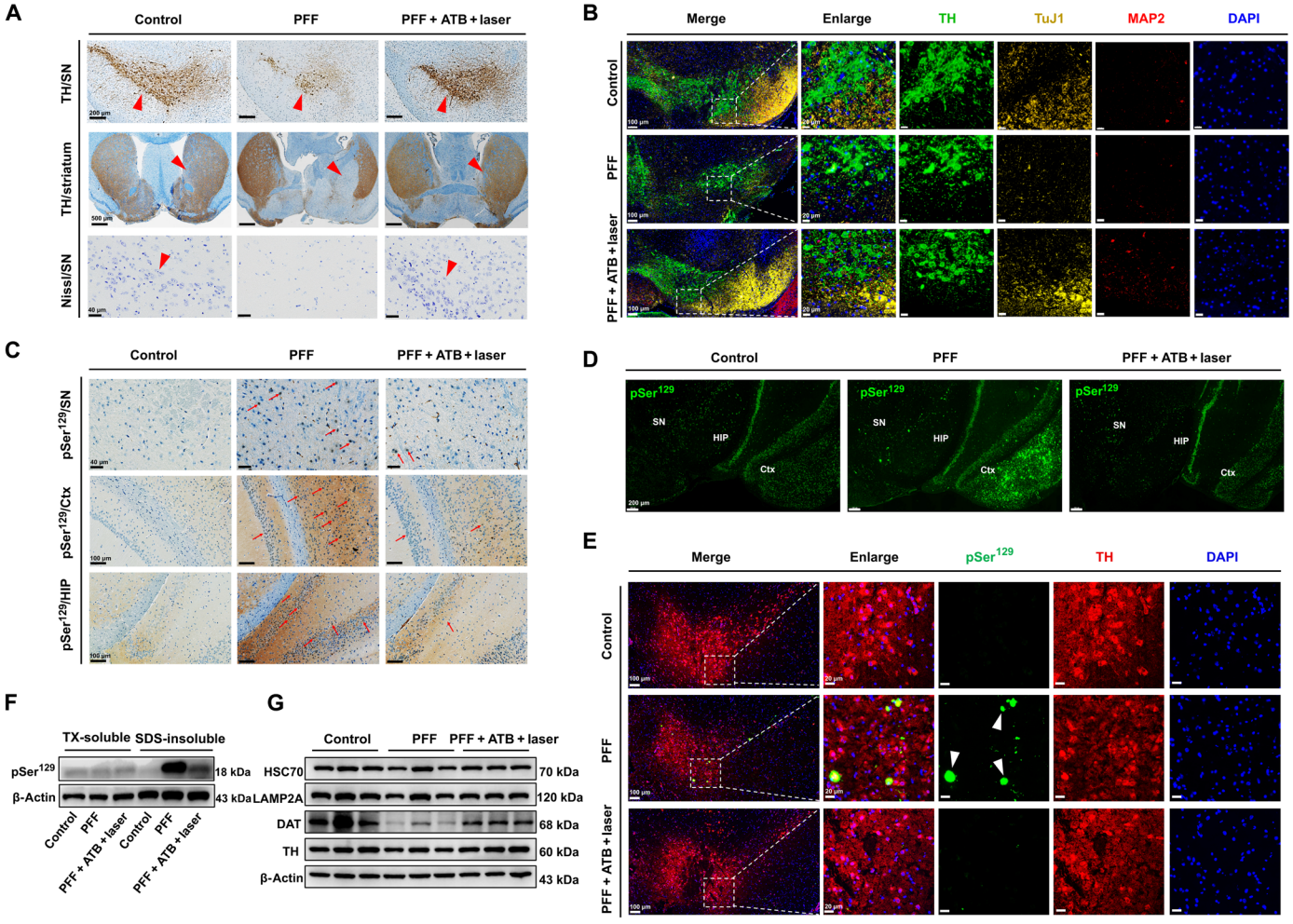

Fig. 5. ATB NP–mediated wireless photothermal DBS alleviates PD in PFF-induced PD mice. (**A**) Representative immunohistochemistry images of TH-positive neurons in the SN and striatum and Nissl-positive neurons in the SN of the coronal mesencephalon sections of control, PFF mice, and PFF mice treated with ATB NPs (1×10^{11}/ml, 5 μl) and NIR laser (1.5 W, 10 ms per pulse, 3 min). Scale bars, 200 μm (top), 40 μm (bottom), and 500 μm (middle). (**B**) Representative immunostaining images of TH, TuJ1, and MAP2 in the SN of coronal mesencephalon sections of control, PFF mice, and PFF mice treated with ATB NPs and NIR laser. Scale bars, 100 μm (merge) and 20 μm (enlarge, TH, TuJ1, MAP2, and DAPI). (**C**) Representative immunohistochemical images of p–α-syn–positive neurons in the SN, cortex, and hippocampus of coronal mesencephalon sections of control, PFF mice, and PFF mice treated with ATB NPs and NIR laser. Scale bars, 40 μm (top) and 100 μm (middle and bottom). Ctx, cortex; HIP, Hippocampus. (**D**) Representative confocal images of p–α-syn–positive neurons in the SN, cortex, and hippocampus of coronal mesencephalon sections of control, PFF mice, and PFF mice treated with ATB NPs and NIR laser. Scale bars, 200 μm. (**E**) Representative confocal images of TH and p–α-syn–positive neurons in the SN of coronal mesencephalon sections of control, PFF mice, and PFF mice treated with ATB NPs and NIR laser. Scale bars, 100 μm (merge) and 20 μm (enlarge, $pSer^{129}$, TH, and DAPI). (**F**) Protein levels of p–α-syn and β-actin from the detergent-soluble and -insoluble fractions from the SN of control, PFF mice, and PFF mice treated with ATB NPs and NIR laser. (**G**) Protein levels of TH, DAT, HSC70, LAMP2A, and β-actin in the SN of control, PFF mice, and PFF mice treated with ATB NPs and NIR laser. All experiments were repeated at least three times.

half-life of about 31 days (*55*), indicating a slow clearance rate for NPs from the brain. Despite this long-term retention, ATB NPs did not show notable toxicity to the brain or overall health in ATB NP–treated mice compared to controls (fig. S16 and tables S2 and S3), underscoring their excellent biosafety profile.

Until now, prior studies have examined the therapeutic effects of NP-based agents on the amelioration of symptoms in mouse models of PD (*27*, *56*–*58*). Among Parkinson's therapeutic approaches, the method of NP administration is pivotal for treatment efficiency. Stereotaxic injection offers several benefits over systemic administration: (i) It provides precise targeting, delivering NPs directly to the affected brain area for concentrated therapeutic impact; (ii) it avoids the blood-brain barrier, a major hurdle for systemic drugs delivery, ensuring that NPs reach their destination without needing to enhance blood-brain barrier permeability, which could be harmful; (iii) it achieves a high local NP concentration with a low dose, potentially boosting treatment effectiveness. Notably, the site of injection for NPs and DBS implementation is also critical in PD treatment. While the subthalamic nucleus (STN) is a Food and Drug Administration–approved target for PD treatment via DBS, its benefits are often compromised by side effects such as cognitive and physiological disturbances (*59*–*62*). In contrast, clinical and animal reports on SN-DBS have highlighted its potential as a promising approach for improving locomotion (*63*–*66*).

In addition, although several studies have demonstrated that nano-based NIR stimulation can successfully evoke the excitation of various neurons, including the sciatic nerve (*67*), dorsal root ganglion neurons (*19*), and auditory neurons (*68*), there have been few reports exploring NP-based photothermal DBS reversing the neuronal damage induced by α-syn aggregates in the SN. In our study, we demonstrated that ATB NP–mediated wireless DBS can completely reverse DA neuron death, with precise spatial control, and restore the locomotor behavior of PD model mice to normal levels (Fig. 6). Once delivered to the target region, ATB NPs were stably retained in the SN and anchored to DA neurons expressing TRPV1 receptors. After pulsed NIR irradiation, the ATB NPs, serving as nanoantennae, mediated NIR light-to-heat conversion, activating the heat-sensitive TRPV1 ion channel on DA neurons to trigger calcium ion influx, depolarization, and action potentials. Meanwhile, the β-syn peptides released from ATB NPs inhibited the formation and promoted the disaggregation of α-syn fibrils. These dynamic processes, coupled with the initiation of chaperone-mediated autophagy, effectively reversed α-syn aggregation in the DA neurons and restored DA levels in the striatum through the nigrostriatal pathway. Ultimately, ATB NP–mediated therapy led to the recovery of locomotor behaviors in PD model mice. The efficacy of this therapy was evident in both PFF- and MPTP-induced PD mice, suggesting its universal applicability. The paradigm we present here offers the following advantages: (i) It leverages the inherent expression of the heat-sensitive TRPV1 receptors in DA neurons of the SN, thereby avoiding the need for brain implantation with a conduit and transgenes; (ii) it ensures precise spatiotemporal control for the degenerated neurons in specific brain area (e.g., SN) with tunable NIR irradiation; (iii) the designed ATB NPs demonstrate excellent biocompatibility to the neurons, SN, whole brain, and living organisms, eliciting no apparent toxicity. Overall, this proof-of-concept study provides valuable insights for future investigations aiming to expand the field of DBS without the need for additional implantation of conduits or genetic manipulation.

MATERIALS AND METHODS

Preparation and characterization of ATB NPs

We first mixed 10 mg of β-syn peptide (Sangon Biotech Co. Ltd., Shanghai) with 7 mg of MPBA (Sigma-Aldrich) in ultradry dimethyl sulfoxide (DMSO) in a three-neck flask. The mixture was stirred at 65°C in an anhydrous and anaerobic atmosphere for 24 hours. The resulting solution was then dialyzed in anhydrous ethanol to remove DMSO and unreacted MPBA and was vacuum dried to obtain the phenylborate ester. We obtained AuNSs with the core SiO_2 and carboxyl surface from commercial source (GSXR150-5 M, nanoComposix). AuNSs were decorated with TRPV1 antibody (K005915P, SolarBio) in accordance with the manufacturer's instructions. In detail, 400 μg of 1-ethyl-3-(3-dimethylaminopropyl)carbodiimide (EDC) and 800 μg of *N*-hydroxysuccinimide (NHS) in sterile PBS solution were added to a 5-ml AuNS solution and allowed to activate for 30 min, followed

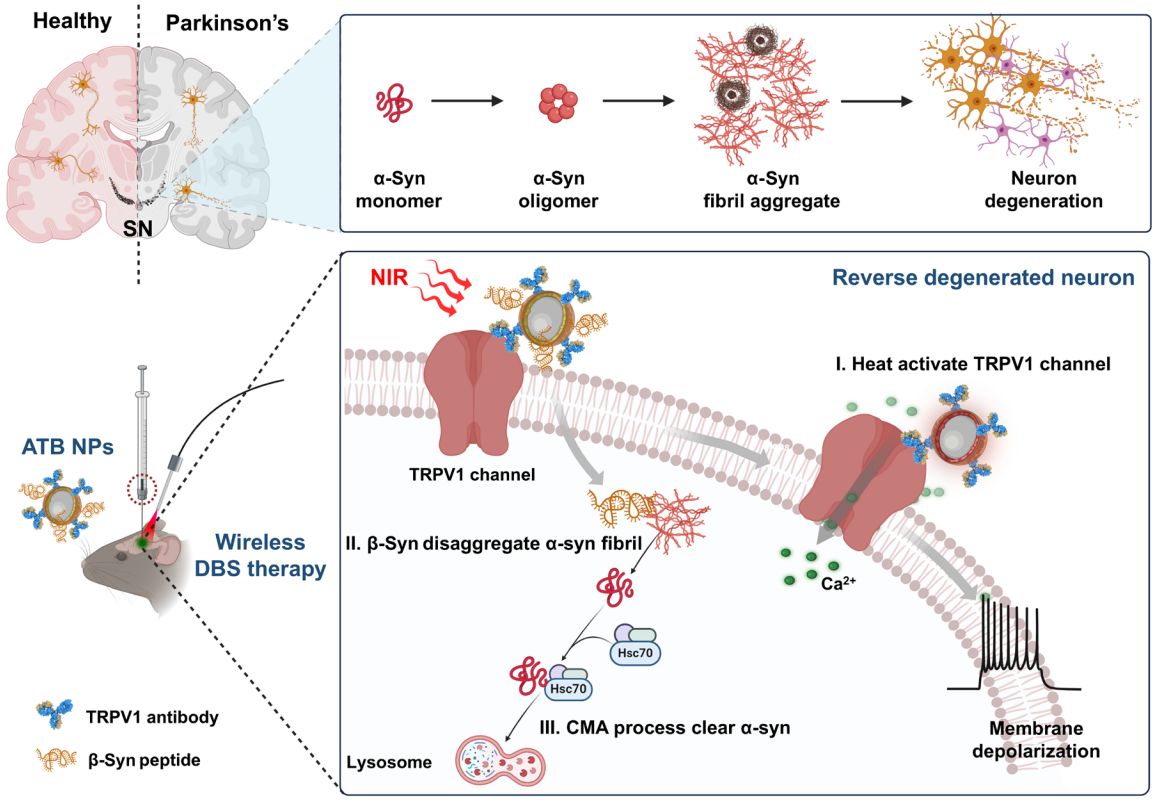

Fig. 6. Working model showing wireless DBS mediated by ATB NPs to reverse PD. (I) Pulsed NIR irradiation triggers the thermal activation of TRPV1 channels and Ca^{2+} influx into neurons to promote membrane depolarization. (II and III) NIR-induced β-syn peptide release into neurons causes a disaggregation of α-syn fibrils, combined with the thermal activation of CMA to clear the pathological α-syn fibrils. This therapy effectively reverses the symptoms of PD. Created using BioRender.com.

by the addition of 150 μg of purified TRPV1 antibody and stirring for 12 hours at room temperature. After centrifuging at 12,000 rpm for 10 min to remove unreacted antibody, 5 mg of the obtained MPBA–β-syn was added to the suspension of AT and stirred overnight. The resulting solution, ATB NPs, was centrifuged at 12,000 rpm for 10 min and resuspended in sterile PBS for storage at 4°C. The particle concentration of ATB NPs was determined by nanoparticle tracking analysis (NanoSight NS300, Malvern Panalytical Ltd.).

To characterize the MPBA, β-syn peptide, and their reaction product, 5 mg of each powder was dissolved in DMSO-d_6 for NMR 1H or 11B spectra measurement (Bruker). The powders were then mixed and ground with KBr particles to form tablets for FTIR measurement. The size and zeta potential of the synthesized gold NPs were determined using a dynamic light scattering (Malvern Zetasizer). In addition, 10 μl of the NPs were adsorbed to carbon-coated copper grids overnight at room temperature for observation via TEM (Ht-7700, Hitachi). The maximum absorption peak of the gold NPs was determined using a UV-visible spectrophotometer. The well-dispersed gold NP solution was diluted to 100 μg/ml and injected into the sample cell for UV-visible spectrum measurement, with a scan range of 350 to 1000 nm. To evaluate the photothermal properties of ATB NPs, a series of solutions were prepared and subjected to NIR irradiation for 5 min, with the change of temperature being observed and recorded via thermal camera every 30 s.

Preparation of α-syn PFF

To produce α-syn PFF, we obtained recombinant α-syn monomers from commercial sources for both mouse (AS-56082, AnaSpec Inc.) and human (S-1001, rPeptide). These monomers were then dissolved in sterile PBS at a concentration of 2 mg/ml and subjected to agitation in an orbital thermomixer at 1000 rpm and 37°C for 7 days. The resulting solution was sonicated for 1 min at 30% amplitude with 1-s intervals to yield the PFF.

Primary culture of dopaminergic neurons

Primary mesencephalon neurons were isolated from the brain of Sprague-Dawley rat embryos (E16, SPF Biotechnology Co. Ltd., Beijing) as previously described protocol with minor modifications (*69*, *70*). In detail, the mesencephalic region of embryos, containing the SN, was rapidly separated. The isolated neurons were then seeded on dishes or glass plates coated with a 0.02% poly-L-ornithine solution (Merck) at a density of 100,000 to 150,000/cm^2 in a medium composed of BrainPhys neuronal medium (05790, STEMCELL Technologies) and SM1 neuronal supplement (05711, STEMCELL Technologies). After culture for 7 days, the dopaminergic neurons reach maturity. Subsequently, they were treated with PFF (2 μg/ml) for 3 days, followed by treatment with ATB NPs (1×10^9/ml) for further experiments.

Immunofluorescence analysis

Primary neurons were first fixed with 4% paraformaldehyde (PFA; SolarBio) for 15 min after treated with ATB and NIR laser. They were then blocked with a solution containing 5% goat serum and 0.3% Triton X-100 in Hanks' balanced salt solution (HBSS; SolarBio) for 45 min, followed by a second block step with 5% goat serum (SolarBio) plus 0.1% Triton X-100 in HBSS for an additional 15 min. Subsequently, the permeated cells were incubated with primary antibodies including anti-TH [58844S, Cell Signaling Technology (CST); 66334-1-Ig, Proteintech), anti-TuJ1 (5568, CST), anti–c-fos (2250T, CST), anti-pα-synSer^{129} (23706, CST), anti-VMAT2 (ab259970, Abcam), anti-TRPV1 (ab203103, Abcam), and anti-MAP2 (ab254144, Abcam) overnight at 4°C. After three washes with HBSS, the cells were incubated with secondary antibodies conjugated with Alexa Fluor 488 or 594 (SolarBio) for 1 hour at room temperature. Last, the fluorescent images were obtained using a Zeiss confocal microscope (UltraVIEW VoX, PerkinElmer) after the coverslips were mounted with antifade mounting medium with 4′,6-diamidino-2-phenylindole (DAPI) (SolarBio).

For in vivo immunofluorescence analysis, mice were perfused with saline solution and 4% PFA, followed by brain isolation and fixation with 4% PFA or immersed in optimal cutting temperature compound and frozen at −20°C overnight. After cryoprotection with 30% sucrose, 10-μm coronal brain sections were prepared using a cryostat. Sections were then blocked with 10% goat serum (SolarBio) in PBS plus 0.3% Triton X-100 and incubated with anti-TH (58844, CST), anti-pα-syn (Ser129) (23706, CST), anti-TRPV1 (ab203103, Abcam), anti–Iba-1 (17198, CST), anti–c-fos (2250T, CST), anti-TuJ1 (5568, CST), or anti-MAP2 (ab254144, Abcam) at 4°C overnight. After washing three times with PBS, floating brain sections were incubated with fluorescein isothiocyanate–conjugated and CY3-conjugated secondary antibodies with 0.1% Triton X-100 and 5% goat serum in PBS for 1 hour at room temperature. Last, the coverslips were scanned, and images were acquired with CaseViewer after mounting with DAPI mounting solution.

Analysis of calcium ion imaging and HEK-293T transfection

The cultured mature neurons were incubated with 2 μM Fluo-4 AM (F14201, Invitrogen) in Dulbecco's modified Eagle's medium for 60 min at 37°C after treatment with PFF (2 μg/ml) and/or ATB NPs (1×10^9/ml). After washing the cells three times with HBSS solution, they were transferred to Dulbecco's modified Eagle's medium for Ca^{2+} imaging. Thermal stimulation was accomplished by irradiating the cells with NIR laser (2 W, 20 ms per pulse, 20 Hz) for 2 min, after 1 min of baseline imaging. In the case of HEK-293T (*Homo sapiens*, human, CRL-11268, American Type Culture Collection) cells, these were transfected with/without human TRPV1 plasmid (HG17498-UT, Sino Biological Inc.; sequencing primer of human TRPV1 plasmid: pCMV3-F, 5′-CAGGTGTCCACTCCCAGGTCCAAG-3′; pcDNA3-R, 5′-GGCAACTAGAAGGCACAGTCGAGG-3), followed by exposure to ATB NPs (1×10^9/ml) for 24 hours. Subsequently, the cells were incubated with Fluo-4 AM and monitored in real time using a Zeiss confocal microscope (PerkinElmer).

Observation of the distribution of ATB NPs in cells

Different modifications of NPs attached to the cells were measured by TEM (Ht-7700, Hitachi). Primary dopaminergic neurons were treated with PFF (2 μg/ml) for 3 days and then incubated with AuNSs, AT NPs, or ATB NPs (1×10^9/ml) for 24 hours once they are mature. Primary cells were collected and fixed overnight at 4°C for ultrathin sections. For HEK-293T cells, they were first transfected with/without human TRPV1 plasmid, followed by treatment with ATB NPs (1×10^9/ml) for 24 hours. Then, cells were collected and fixed overnight at 4°C for ultrathin sections. All the sections were observed under TEM, and images were captured by charge-coupled device camera.

To further confirm the role of TRPV1 in the binding of ATB NPs to cell membranes, the cultured mature primary neurons were first blocked with TRPV1 primary antibody (1 μg/ml) for 3 hours. After incubation with ATB NPs (1×10^9/ml) for 24 hours, cells were rinsed

with PBS and fixed for 15 min. After incubation with primary antibody of TRPV1 (A00128-4, Boster Biological Technology) and Alexa Fluor 488–conjugated secondary antibody (A0423, Beyotime), the cells were washed with PBS and observed by laser reflection technology of confocal laser scanning microscope (STELLARIS 8, Leica).

To examine the localization of ATB NPs in the nearby phagocytes in vitro, we isolated and cultured primary mesencephalic cells from 16-day-old embryos for 7 days without 5-fluoro-2′-deoxyuridine (F0503, Sigma-Aldrich) to inhibit glial cell growth. We then treated the cells with ATB NPs (1×10^9/ml) for 24 hours, followed by rinsing with PBS. The cells were incubated with Iba-1 (17198, CST) or GFAP antibodies (53-9892-82, eBiosciences) to mark microglia and astrocytes, respectively. The cells were observed by laser reflection.

Electrophysiological recording in vitro

Thermal activation of primary dopaminergic neurons or HEK-293T transfect with TRPV1 plasmid was detected by electrophysiology as previously described (*71*, *72*). Neuronal cells were seeded on the poly-L-ornithine–coated glass coverlids, treated with PFF (2 μg/ml) for 3 days, and then incubated with ATB NPs (1×10^9/ml) for 24 hours upon maturation. The coverlids were subsequently transferred to an extracellular solution (pH 7.2 to 7.4) containing 129 mM NaCl, 5 mM KCl, 1 mM $MgCl_2$, 2 mM $CaCl_2$, 25 mM Hepes, and 30 mM D-glucose. Glass electrodes filled with intracellular solution (pH 7.2 to 7.4) comprising 110 mM potassium gluconate, 20 mM KCl, 5 mM $MgCl_2$, 20 mM Hepes, 7 mM creatine sodium, 0.6 mM EGTA, 2 mM Na_3 adenosine triphosphate, and 0.2 mM Na_3 guanosine triphosphate were gradually attached to the cellular membrane to form a perfusion system before stimulation. Cells were held at −70 mV to record the action potential evoked by NIR laser (20 Hz, 2 W, 20 ms per pulse). For recording TRPV1-induced currents, HEK-293T cells were transfected with human TRPV1 plasmid, treated with ATB NPs (1×10^9/ml) for 24 hours, and then placed in an extracellular solution (pH 7.2 to 7.4) containing 125 mM NaCl, 2 mM KCl, 2 mM $MgCl_2$, 2 mM $CaCl_2$, 25 mM Hepes, and 51 mM D-glucose. A glass pipette filled with intracellular solution (pH 7.2 to 7.4) containing 142 mM potassium gluconate, 2 mM KCl, 4 mM $MgCl_2$, 10 mM Hepes, 7 mM creatine sodium, 0.2 mM EGTA, and 4 mM Na_3 adenosine triphosphate was positioned near the cells to form a perfusion system. The inward currents in response to NIR stimulation were recorded using a MultiClamp 700B amplifier.

Measurement of β-syn peptide to depolymerize α-syn fibrils or prevent α-syn aggregation

To assess the capability of the β-syn peptides to promote the degradation of α-syn fibrils, a solution of 25 μl of PFF fibrils (2 mg/ml) mixed with 25 μl of β-syn peptide (5 mg/ml) was subjected to shaking in an orbital thermomixer at 1000 rpm and 37°C. The resulting mixture was then diluted 100 times for standard typical ThT (T3516, Sigma-Aldrich) assay at specified time point (0, 6, 12, 24, 72, and 168 hours). Normally, ThT is commonly used to detect the presence of amyloid-like fibers with its fluorescence signal markedly amplified upon binding to amyloid fibers. The intensity of ThT was measured at 482 nm (excitation, 450 nm) using a fluorescence spectrophotometer after the addition of ThT solution to achieve a final concentration of 25 μM.

In addition, TEM was used to visualize the morphological changes in PFF following their mixing with the β-syn peptides. Specifically, 10 μl of the mixture at each time point was applied to copper grids, left to adsorb for 10 min at room temperature, and then rinsed with three drops of PBS. Subsequently, the grids were then incubated with 10 μl of 10% uranyl acetate for 20 min, followed by rinsing and drying before imaging with TEM (Ht-7700; 80 kV).

To observe the depolymerization of α-syn fibrils, samples collected at each time point were subjected to BN-PAGE 4 to 16% bis-tris gels (RTD6139-0416, Real-Times Biotechnology) according to the manufacturer's instruction. Specifically, 15 μl of the mixture containing proteins was loaded onto the BN-PAGE gels, and then cathode buffer containing 50 mM tricine, 15 mM bis-tris, and 0.002% brilliant blue G-250 and anode buffer containing 50 mM tricine and 15 mM bis-tris were used for electrophoresis at 120 V for 120 min. The gels were then stained with Coomassie brilliant blue and imaged using a ChemiDoc MP Imaging System (Bio-Rad). Similarly, the ability of the β-syn peptides to inhibit the aggregation of α-syn was evaluated following the same protocols.

Binding affinity measurement of β-syn peptide to α-syn fibrils

Binding affinity of β-syn peptide to α-syn fibrils was determined by MicroCal PEAQ-ITC (Malvern Panalytical Ltd.) isothermal calorimeter. β-syn peptides were first diluted to 14 μM in PBS and injected into reaction cell. Then, a total of 40 μl of 140 μM α-syn PFFs were dropped 19 times into the reaction cell with 2-μl injection each time. The obtained titration curve and thermodynamic data were analyzed by MicroCal PEAQ-ITC analyzer software (Malvern Panalytical Ltd.)

Binding affinity measurement between α-syn monomers

We used the MicroScale Thermophoresis (NanoTemper) to test binding affinity of α-syn monomer toward each other. First, the Lys and Arg within α-syn monomer were labeled with fluorescent dyes (MO-L011, RED-NHS). Then, 6 μl of a range of concentrations of unlabeled α-syn monomer (from 143 to 0.00436 μM) was mixed with same volume of 20 nM labeled α-syn monomer, followed by detecting the movement of proteins in a microscopic temperature gradient field to qualify their interaction. The obtained dynamic data were analyzed by MO.Affinity Analysis.

Western blotting analysis

Cells treated with PFF (2 μg/ml) were incubated with ATB NPs (1×10^9/ml) for 24 hours, followed by exposure to NIR laser (2 W, 20 ms per pulse, 20 Hz) for 1 min. After 24 hours, dopaminergic cells were collected and lysed by radioimmunoprecipitation assay lysis and extraction buffer (Thermo Fisher Scientific) containing phosphatase inhibitor (all-in-one, SolarBio) and protease inhibitor cocktail (Roche). After sonication for 30 s (30% amplitude, 10-s on, 10-s off), homogenized samples were centrifuged at 12,000 rpm for 10 min, and the supernatants were collected for immunoblot. After quantification by bicinchoninic acid and heat-inactivation, 10 to 20 μg of proteins were loaded on the 10 or 12% SDS-PAGE gels for electrophoresis at 90 V for 120 min, followed by transfer to the polyvinylidene difluoride membranes (Millipore). Then, the membranes were blocked with 5% skim milk or bovine serum albumin in TBST solution (tris-buffered saline with 0.1% Tween 20) at room temperature for 1 hour. Protein bands were incubated with primary antibodies including anti-TH (58844, CST), anti-Hsc70 (ab51052, Abcam), anti-LAMP2A (ab125068, Abcam), anti-TRPV1 (ab203103, Abcam), anti-TuJ1 (5568, CST), anti-DAT (22524-1-AP, Proteintech), anti-VMAT2 (ab259970, Abcam), and anti–β-actin (TA-09, ZSGB-BIO)

at 4°C overnight. After three washes with TBST, protein bands were incubated with horseradish peroxidase–conjugated rabbit or mouse secondary antibodies (ZSGB-BIO) at room temperature for 2 hours, followed by visualization via ChemiDoc MP Imaging System (Bio-Rad).

For measurement the protein level of p–α-syn, cellular lysates were prepared using lysis buffer composed of 10 mM tris-HCl (pH 7.4), 150 mM NaCl, 5 mM EDTA, 1% Triton X-100, phosphatase inhibitor, and protease inhibitor cocktail. Soluble supernatants were obtained after centrifugation at 4°C and 12,000 rpm for 10 min, followed by the addition of lysis buffer containing 2% SDS to the insoluble pellets. After sonication and centrifugation, supernatants with insoluble PFF were collected for immunoblot. The protein bands were incubated with primary antibodies including pα-syn (Ser129) (23706, CST), and anti–β-actin (ZSGB-BIO) at 4°C overnight.

Tissue total lysates were prepared by homogenization in radioimmunoprecipitation assay lysis and extraction buffer containing phosphatase inhibitor and protease inhibitor cocktail. After sonication and centrifugation, the supernatants were collected for immunoblot. The soluble and insoluble fractions of tissue lysates were prepared following the protocols of cellular lysates.

Animal experiment with stereotactic injection and treatment

Male C57BL/6J mice (12 weeks old, ~25 g) were purchased from SPF Biotechnology Co. Ltd. (Beijing, China). All animal experiments were performed in accordance with the Institutional Animal Care and Use Committee of National Center for Nanoscience and Technology (ethical approval number: NCNST21-2407-0606). The mice were bred in the specific pathogen–free animal facility in a temperature-controlled (22°C) environment under a strict 12-hour light cycle and fed a standard, autoclaved chow diet and water ad libitum at 50 to 60% relative humidity, with the cages changed every 2 days. Before experiments, the mice were kept in the specific pathogen–free animal facility for a 7-day acclimation period. C57BL/6J mice (12 weeks old) were used for intrastriatal delivery of α-syn PFF to prepare PD models following standard stereotaxic surgery methods as following: Mice were first anesthetized by isoflurane anesthetic and injected with 2 μl of PBS or PFF (5 μg/2 μl) using a 10-μl Hamilton microsyringe (Hamilton) by a stereotaxic instrument (KEW BASIS Biotechnology Co. Ltd., Nanjing) at referenced coordinates [anteroposterior (AP), +0.2 mm; mediolateral (ML), +2.0 mm from bregma; dorsoventral (DV), −2.6 mm]. Mice was sutured and kept for 3 months, followed by stereotaxic injection with 5 μl of PBS or ATB NPs (1×10^{11}/ml) in the SN (AP, −3.5 mm; ML, ±1.25 mm from bregma; DV, −4.3 mm). After 1 day, mice were anesthetized by isoflurane anesthetic and treated with pulsed NIR laser. The tip of laser emitting fiber was placed 1 cm above the mouse skull and irradiated vertically at the injection site for 3 min (1.5 W, 10 ms per pulse, 20 Hz).

LA-ICP-MS and ICP-MS analysis

C57BL/6J mice were injected with ATB NPs (1×10^{11}/ml) into the SN and the coronal brain slices with 60 μm were prepared and traced with the Au element (phosphorus element was used to illustrate the shape of the mice brain) in situ via laser ablation after 24 hours, as determined by previously reported procedure (*73*). The LA system (PhotonMachines Analyte HE with 193-nm ArF excimer) combined with ICP-MS (Agilent 7900) was used in an atmosphere of ultra high purity He (0.9 liter/min) mixed with Ar (0.87 liter/min), and the spot energy was 2.76 J/cm^2 with 20 Hz. NIST 610 was used as an external standard.

To quantify the distribution of ATB NPs in brain regions and other tissues or body fluids, C57BL/6J mice were injected with ATB NPs (1×10^{11}/ml) into the SN and kept for 8 weeks. At the time point of 0 hours, 3 weeks, 5 weeks, and 8 weeks, the brain was isolated and different regions (olfactory, cortex, striatum, hippocampus, SN, hindbrain, and midbrain except SN) were separated and weighed for ICP-MS quantification. Other tissues (heart, liver, spleen, lung, and kidney) and feces or body fluids (blood, urine, and cerebrospinal fluid) were collected or weighed. The gold content in the obtained samples was measured by ICP-MS (Thermo-X7, Thermo Fisher Scientific) after dissolving the tissues in nitric acid and aqua regia (metal–oxide–semiconductor grade) at high temperature.

Determination of DA release in mice

Mice were initially administered bilateral injections of ATB NPs into the SN for 24 hours. Subsequently, they were anesthetized with isoflurane and placed in a stereotaxic instrument for FSCV recording. A carbon fiber electrode was then stereotactically implanted into the caudate putamen (striatum; coordinates: AP, +0.2 mm; ML, +2.0 mm; DV, −2.6 mm) and maintained for a few minutes. A reference electrode (Ag/AgCl electrode) was placed on the surface of moist surface of the skull to form a circuit. Once an optical fiber with NIR laser delivered into the SN for 3 min, the FSCV spectra were recorded using an electrochemical analyzer (Zensor).

Animal behavior measurements

The motor abilities of mice were assessed using the rotarod test, following a 1-week training period. This involved placing the mice on a 3-cm-diameter rotarod, which accelerated from 5 to 50 rpm over 5 min, with the latency time recorded for three trials. In addition, the pole test was conducted after a week of training, where the time taken for the mice to crawl down a 75-cm-long, 1-cm-diameter pole was recorded for three trials. The open field test was used to evaluate locomotor activity and exploratory behavior. Mice were given 2 min to adapt to a 50-cm by 50-cm by 40-cm open area before a 5-min free exploration period, during which their movement path and the number of times they crossed the middle square were recorded. The open area was cleaned with 70% alcohol between trials to minimize interference.

Immunohistochemistry analysis

Mice were perfused with saline solution and 4% PFA, followed by brain isolation and fixation with 4% PFA overnight. After cryoprotection with 30% sucrose, 10-μm coronal brain sections were prepared using a cryostat. Sections were incubated with anti-TH (58844, CST) or anti-pS129–α-syn (23706, CST) with 5% normal donkey serum, 0.1% Triton X-100 containing PBS blocking solution. The sections were then incubated with streptavidin-conjugated horseradish peroxidase and biotinylated secondary antibodies. Immune-positive signals were visualized using a 3,3′-diaminobenzidine (DAB) kit.

In vivo cell viability analysis by flow cytometry

C57BL/6J male mice were first administered bilateral injections of ATB NPs into the SN for 24 hours, followed by NIR laser treatment (1.5 W, 10 ms per pulse) for 3 min under the anesthesia. After 24 hours, mice were euthanized, and their SN tissues were immediately

isolated. The tissues were prepared into single-cell suspension by mechanical grinding. After centrifugation, cells were incubated with phycoerythrin anti-mouse CD11b antibody (50-0112-U025, Tonbo Biosciences) and fluorescein isothiocyanate anti-mouse CD45 antibody (35-0451-U025, Tonbo Biosciences) for 1 hour at room temperature to mark microglia, with Alexa Fluor 488–conjugated GFAP (53-9892-82, eBiosciences) for 1 hour at room temperature to mark astrocyte. After centrifugation to remove the antibody, the viability of cells was then determined and analyzed using 7-Aminoactinomycin D (7AAD) staining solution (00-6993-50, eBiosciences) by flow cytometry (CytoFLEX S, Beckman Coulter). For TH neurons and TRPV1 neurons, cells were first stained with 7AAD for 15 min, followed by centrifugation and fixation with 1× Fix/Perm buffer (TNB-1020-L050, Tonbo Biosciences) at room temperature for 30 min. Then, cells were incubated with 1× Flow Cytometry Perm Buffer (TNB-1213-L150, Tonbo Biosciences) for another 15 min. Afterward, cells were incubated with TH primary antibody (58844, CST) or TRPV1 antibody (ab203103, Abcam) at room temperature for 1 hour, followed by centrifugation and incubation with secondary antibodies conjugated with Alexa Fluor 488 (A0423, Beyotime) for another 1 hour. After centrifugation to remove the antibody, the cell viability was then determined by flow cytometry (CytoFLEX S, Beckman Coulter) and analyzed by FlowJo VX software.

Statistical analysis and reproducibility

The data are presented as the means ± SD, and differences between the two groups were analyzed by a two-tailed unpaired *t* test. In addition, differences among multiple groups were analyzed using a two-tailed one-way analysis of variance (ANOVA) with GraphPad Prism software (v.8.0). Statistical significance was set at $^{*}P < 0.05$, $^{**}P < 0.01$, $^{***}P < 0.001$, and $^{****}P < 0.0001$. All animal and in vitro experiments were repeated at least three times unless stated otherwise.

Supplementary Materials

The PDF file includes:
Supplementary Text
Figs. S1 to S16
Tables S1 to S3
Legends for movies S1 to S6

Other Supplementary Material for this manuscript includes the following:
Movies S1 to S6

REFERENCES AND NOTES

1. W. Poewe, K. Seppi, C. M. Tanner, G. M. Halliday, P. Brundin, J. Volkmann, A.-E. Schrag, A. E. Lang, Parkinson disease. *Nat. Rev. Dis. Primers.* **3**, 17013 (2017).
2. Y. Smith, T. Wichmann, S. A. Factor, M. R. DeLong, Parkinson's disease therapeutics: New developments and challenges since the introduction of levodopa. *Neuropsychopharmacology* **37**, 213–246 (2011).
3. D. Charvin, R. Medori, R. A. Hauser, O. Rascol, Therapeutic strategies for Parkinson disease: Beyond dopaminergic drugs. *Nat. Rev. Drug Discov.* **17**, 804–822 (2018).
4. C. Gasca-Salas, B. Fernández-Rodríguez, J. A. Pineda-Pardo, R. Rodríguez-Rojas, I. Obeso, F. Hernández-Fernández, M. del Álamo, D. Mata, P. Guida, C. Ordás-Bandera, J. I. Montero-Roblas, R. Martínez-Fernández, G. Foffani, I. Rachmilevitch, J. A. Obeso, Blood-brain barrier opening with focused ultrasound in Parkinson's disease dementia. *Nat. Commun.* **12**, 779 (2021).
5. R. Chen, A. Canales, P. Anikeeva, Neural recording and modulation technologies. *Nat. Rev. Mater.* **2**, 16093 (2017).
6. F. Darlot, C. Moro, N. El Massri, C. Chabrol, D. M. Johnstone, F. Reinhart, D. Agay, N. Torres, D. Bekha, V. Auboiroux, T. Costecalde, C. L. Peoples, H. D. T. Anastascio, V. E. Shaw, J. Stone, J. Mitrofanis, A.-L. Benabid, Near-infrared light is neuroprotective in a monkey model of Parkinson disease. *Ann. Neurol.* **79**, 59–75 (2016).
7. N. Yu, L. Huang, Y. Zhou, T. Xue, Z. Chen, G. Han, Near-infrared-light activatable nanoparticles for deep-tissue-penetrating wireless optogenetics. *Adv. Healthc. Mater.* **8**, 1801132 (2019).
8. D. M. Johnstone, K. Coleman, C. Moro, N. Torres, J. T. Eells, G. E. Baker, K. Ashkan, J. Stone, A.-L. Benabid, J. Mitrofanis, The potential of light therapy in Parkinson's disease. *Chronophysiol. Ther.* **4**, 1–14 (2014).
9. M. G. Shapiro, K. Homma, S. Villarreal, C.-P. Richter, F. Bezanilla, Infrared light excites cells by changing their electrical capacitance. *Nat. Commun.* **3**, 736 (2012).
10. J. L. Carvalho-de-Souza, J. S. Treger, B. Dang, S. B. H. Kent, D. R. Pepperberg, F. Bezanilla, Photosensitivity of neurons enabled by cell-targeted gold nanoparticles. *Neuron* **86**, 207–217 (2015).
11. E. Pastrana, Optogenetics: Controlling cell function with light. *Nat. Methods* **8**, 24–25 (2011).
12. E. S. Boyden, F. Zhang, E. Bamberg, G. Nagel, K. Deisseroth, Millisecond-timescale, genetically targeted optical control of neural activity. *Nat. Neurosci.* **8**, 1263–1268 (2005).
13. M. S. Keiser, P. T. Ranum, C. M. Yrigollen, E. M. Carrell, G. R. Smith, A. L. Muehlmatt, Y. H. Chen, J. M. Stein, R. L. Wolf, E. Radaelli, T. J. Lucas II, P. Gonzalez-Alegre, B. L. Davidson, Toxicity after AAV delivery of RNAi expression constructs into nonhuman primate brain. *Nat. Med.* **27**, 1982–1989 (2021).
14. D. Martins, I. Tavares, C. Morgado, "Hotheaded": The role of TRPV1 in brain functions. *Neuropharmacology* **85**, 151–157 (2014).
15. E. Mezey, Z. E. Toth, D. N. Cortright, M. K. Arzubi, J. E. Krause, R. Elde, A. Guo, P. M. Blumberg, A. Szallasi, Distribution of mRNA for vanilloid receptor subtype 1 (VR1), and VR1-like immunoreactivity, in the central nervous system of the rat and human. *Proc. Natl. Acad. Sci. U.S.A.* **97**, 3655–3660 (2000).
16. A. Szallasi, D. N. Cortright, C. A. Blum, S. R. Eid, The vanilloid receptor TRPV1: 10 years from channel cloning to antagonist proof-of-concept. *Nat. Rev. Drug Discov.* **6**, 357–372 (2007).
17. J. A. Kauer, H. E. Gibson, Hot flash: TRPV channels in the brain. *Trends Neurosci.* **32**, 215–224 (2009).
18. H. Huang, S. Delikanli, H. Zeng, D. M. Ferkey, A. Pralle, Remote control of ion channels and neurons through magnetic-field heating of nanoparticles. *Nat. Nanotechnol.* **5**, 602–606 (2010).
19. H. Nakatsuji, T. Numata, N. Morone, S. Kaneko, Y. Mori, H. Imahori, T. Murakami, Thermosensitive ion channel activation in single neuronal cells by using surface-engineered plasmonic nanoparticles. *Angew. Chem. Int. Ed.* **54**, 11725–11729 (2015).
20. R. Chen, G. Romero, M. G. Christiansen, A. Mohr, P. Anikeeva, Wireless magnetothermal deep brain stimulation. *Science* **347**, 1477–1480 (2015).
21. D. Rosenfeld, A. W. Senko, J. Moon, I. Yick, G. Varnavides, D. Gregureć, F. Koehler, P.-H. Chiang, M. G. Christiansen, L. Y. Maeng, A. S. Widge, P. Anikeeva, Transgene-free remote magnetothermal regulation of adrenal hormones. *Sci. Adv.* **6**, eaaz3734 (2020).
22. D. Nelidova, R. K. Morikawa, C. S. Cowan, Z. Raics, D. Goldblum, H. P. N. Scholl, T. Szikra, A. Szabo, D. Hillier, B. Roska, Restoring light sensitivity using tunable near-infrared sensors. *Science* **368**, 1108–1113 (2020).
23. A. D. Guler, A. Rainwater, J. G. Parker, G. L. Jones, E. Argilli, B. R. Arenkiel, M. D. Ehlers, A. Bonci, L. S. Zweifel, R. D. Palmiter, Transient activation of specific neurons in mice by selective expression of the capsaicin receptor. *Nat. Commun.* **3**, 746 (2012).
24. L. Chen, M. B. Feany, α-Synuclein phosphorylation controls neurotoxicity and inclusion formation in a *Drosophila* model of Parkinson disease. *Nat. Neurosci.* **8**, 657–663 (2005).
25. C. Soto, S. Pritzkow, Protein misfolding, aggregation, and conformational strains in neurodegenerative diseases. *Nat. Neurosci.* **21**, 1332–1340 (2018).
26. E. Nordström, F. Eriksson, J. Sigvardson, M. Johannesson, A. Kasrayan, M. Jones-Kostalla, P. Appelkvist, L. Söderberg, P. Nygren, M. Blom, A. Rachalski, K. Nordenankar, O. Zachrisson, E. Amandius, G. Osswald, M. Moge, M. Ingelsson, J. Bergström, L. Lannfelt, C. Möller, M. G. et Johanna Fälting, ABBV-0805, a novel antibody selective for soluble aggregated alpha-synuclein, prolongs lifespan and prevents buildup of α-synuclein pathology in mouse models of Parkinson's disease. *Neurobiol. Dis.* **161**, 105543 (2021).
27. D. Kim, J. M. Yoo, H. Hwang, J. Lee, S. H. Lee, S. P. Yun, M. J. Park, M. Lee, S. Choi, S.-H. Kwon, S. Lee, S. H. Kwon, S. Kim, Y. J. Park, M. Kinoshita, Y.-H. Lee, S. Shin, S. R. Paik, S. J. Lee, S. Lee, B. H. Hong, H. S. Ko, Graphene quantum dots prevent α-synucleinopathy in Parkinson's disease. *Nat. Nanotechnol.* **13**, 812–818 (2018).
28. H. Mohammad-Beigi, A. Hosseini, M. Adeli, M. R. Ejtehadi, G. Christiansen, C. Sahin, Z. Tu, M. Tavakol, A. Dilmaghani-Marand, I. Nabipour, F. Farzadfar, D. E. Otzen, M. Mahmoudi, M. J. Hajipour, Mechanistic understanding of the interactions between nano-objects with different surface properties and α-synuclein. *ACS Nano* **13**, 3243–3256 (2019).
29. Y. Sun, A. Kakinen, C. Zhang, Y. Yang, A. Faridi, T. P. Davis, W. Cao, P. C. Ke, F. Ding, Amphiphilic surface chemistry of fullerenols is necessary for inhibiting the amyloid aggregation of alpha-synuclein NACore. *Nanoscale* **11**, 11933–11945 (2019).
30. B. Dehay, J. Bove, N. Rodriguez-Muela, C. Perier, A. Recasens, P. Boya, M. Vila, Pathogenic lysosomal depletion in Parkinson's disease. *J. Neurosci.* **30**, 12535–12544 (2010).
31. T. Moors, S. Paciotti, D. Chiasserini, P. Calabresi, L. Parnetti, T. Beccari, W. D. J. van de Berg, Lysosomal dysfunction and α-synuclein aggregation in Parkinson's disease: Diagnostic links. *Mov. Disord.* **31**, 791–801 (2016).

32. A. R. Rastinehad, H. Anastos, E. Wajswol, J. S. Winoker, J. P. Sfakianos, S. K. Doppalapudi, M. R. Carrick, C. J. Knauer, B. Taouli, S. C. Lewis, A. K. Tewari, J. A. Schwartz, S. E. Canfield, A. K. George, J. L. West, N. J. Halas, Gold nanoshell-localized photothermal ablation of prostate tumors in a clinical pilot device study. *Proc. Natl. Acad. Sci. U.S.A.* **116**, 18590–18596 (2019).
33. A. Marino, S. Arai, Y. Hou, A. Degl'Innocenti, V. Cappello, B. Mazzolai, Y.-T. Chang, V. Mattoli, M. Suzuki, G. Ciofani, Gold nanoshell-mediated remote myotube activation. *ACS Nano* **11**, 2494–2508 (2017).
34. J. Li, J. Liu, C. Chen, Remote control and modulation of cellular events by plasmonic gold nanoparticles: Implications and opportunities for biomedical applications. *ACS Nano* **11**, 2403–2409 (2017).
35. H. Xin, B. Namgung, L. P. Lee, Nanoplasmonic optical antennas for life sciences and medicine. *Nat. Rev. Mater.* **3**, 228–243 (2018).
36. A. Qu, X. Wu, S. Li, M. Sun, L. Xu, H. Kuang, C. Xu, An NIR-responsive DNA-mediated nanotetrahedron enhances the clearance of senescent cells. *Adv. Mater.* **32**, 2000184 (2020).
37. E. Aznar, M. D. Marcos, R. Martínez-Máñez, F. Sancenón, J. Soto, P. Amorós, C. Guillem, pH- and photo-switched release of guest molecules from mesoporous silica supports. *J. Am. Chem. Soc.* **131**, 6833–6843 (2009).
38. R. Shaltiel-Karyo, M. Frenkel-Pinter, N. Egoz-Matia, A. Frydman-Marom, D. E. Shalev, D. Segal, E. Gazit, Inhibiting α-synuclein oligomerization by stable cell-penetrating β-synuclein fragments recovers phenotype of Parkinson's disease model flies. *PLOS ONE* **5**, e13863 (2010).
39. D. Baimanov, J. Wu, R. Chu, R. Cai, B. Wang, M. Cao, Y. Tao, J. Liu, M. Guo, J. Wang, X. Yuan, C. Ji, Y. Zhao, W. Feng, L. Wang, C. Chen, Immunological responses induced by blood protein coronas on two-dimensional MoS_2 nanosheets. *ACS Nano* **14**, 5529–5542 (2020).
40. P. D. Ross, S. Subramanian, Thermodynamics of protein association reactions forces contributing to stability. *Biochemistry* **20**, 3096–3102 (1981).
41. E. Gazit, A possible role for π-stacking in the self-assembly of amyloid fibrils. *FASEB J.* **16**, 77–83 (2002).
42. Y. Zhou, Y. Yao, Z. Yang, Y. Tang, G. Wei, Naphthoquinone–dopamine hybrids disrupt α-synuclein fibrils by their intramolecular synergistic interactions with fibrils and display a better effect on fibril disruption. *Phys. Chem. Chem. Phys.* **25**, 14471–14483 (2023).
43. H.-J. Lee, J.-E. Suk, E.-J. Bae, J.-H. Lee, S. R. Paik, S.-J. Lee, Assembly-dependent endocytosis and clearance of extracellular a-synuclein. *Int. J. Biochem. Cell Biol.* **40**, 1835–1849 (2008).
44. J. W. P. Brown, A. K. Buell, T. C. T. Michaels, G. Meisl, J. Carozza, P. Flagmeier, M. Vendruscolo, T. P. J. Knowles, C. M. Dobson, C. Galvagnion, β-Synuclein suppresses both the initiation and amplification steps of α-synuclein aggregation via competitive binding to surfaces. *Sci. Rep.* **6**, 36010 (2016).
45. D. M. Johnstone, C. Moro, J. Stone, A.-L. Benabid, J. Mitrofanis, Turning on lights to stop neurodegeneration: The potential of near infrared light therapy in Alzheimer's and Parkinson's disease. *Front. Neurosci.* **9**, 500 (2016).
46. C. Paviolo, J. W. Haycock, J. Yong, A. Yu, P. R. Stoddart, S. L. McArthur, Laser exposure of gold nanorods can increase neuronal cell outgrowth. *Biotechnol. Bioeng.* **110**, 2277–2291 (2013).
47. K. Fifel, A. Videnovic, Light therapy in Parkinson's disease: Towards mechanism-based protocols. *Trends Neurosci.* **41**, 252–254 (2018).
48. A. Qu, M. Sun, J.-Y. Kim, L. Xu, C. Hao, W. Ma, X. Wu, X. Liu, H. Kuang, N. A. Kotov, C. Xu, Stimulation of neural stem cell differentiation by circularly polarized light transduced by chiral nanoassemblies. *Nat. Biomed. Eng.* **5**, 103–113 (2021).
49. J. Liu, C. Liu, J. Zhang, Y. Zhang, K. Liu, J.-X. Song, S. G. Sreenivasmurthy, Z. Wang, Y. Shi, C. Chu, Y. Zhang, C. Wu, X. Deng, X. Liu, J. Song, R. Zhuang, S. Huang, P. Zhang, M. Li, L. Wen, Y. W. Zhang, G. Liu, A self-assembled α-synuclein nanoscavenger for Parkinson's disease. *ACS Nano* **14**, 1533–1549 (2020).
50. L. Wang, Q. Sun, X. Wang, T. Wen, J.-J. Yin, P. Wang, R. Bai, X.-Q. Zhang, L.-H. Zhang, A.-H. Lu, C. Chen, Using hollow carbon nanospheres as a light-induced free radical generator to overcome chemotherapy resistance. *J. Am. Chem. Soc.* **137**, 1947–1955 (2015).
51. B. Dehay, M. Bourdenx, P. Gorry, S. Przedborski, M. Vila, S. Hunot, A. Singleton, C. W. Olanow, K. M. Merchant, E. Bezard, G. A. Petsko, W. G. Meissner, Targeting α-synuclein for treatment of Parkinson's disease: Mechanistic and therapeutic considerations. *Lancet Neurol.* **14**, 855–866 (2015).
52. K. C. Luk, I. P. Mills, J. Q. Trojanowski, V. M.-Y. Lee, Interactions between Hsp70 and the hydrophobic core of α-synuclein inhibit fibril assembly. *Biochemistry* **47**, 12614–12625 (2008).
53. B. Boland, W. H. Yu, O. Corti, B. Mollereau, A. Henriques, E. Bezard, G. M. Pastores, D. C. Rubinsztein, R. A. Nixon, M. R. Duchen, G. R. Mallucci, G. Kroemer, B. Levine, E. L. Eskelinen, F. Mochel, M. Spedding, C. Louis, O. R. Martin, M. J. Millan, Promoting the clearance of neurotoxic proteins in neurodegenerative disorders of ageing. *Nat. Rev. Drug Discov.* **17**, 660–688 (2018).
54. S. Hickman, S. Izzy, P. Sen, L. Morsett, J. El Khoury, Microglia in neurodegeneration. *Nat. Neurosci.* **21**, 1359–1369 (2018).
55. J. Gao, Q. Song, X. Gu, G. Jiang, J. Huang, Y. Tang, R. Yu, A. Wang, Y. Huang, G. Zheng, H. Chen, X. Gao, Intracerebral fate of organic and inorganic nanoparticles is dependent on microglial extracellular vesicle function. *Nat. Nanotechnol.* **19**, 376–386 (2023).
56. W. Jiang, Q. Li, R. Zhang, J. Li, Q. Lin, J. Li, X. Zhou, X. Yan, K. Fan, Chiral metal-organic frameworks incorporating nanozymes as neuroinflammation inhibitors for managing Parkinson's disease. *Nat. Commun.* **14**, 8137 (2023).
57. H. Liu, Y. Han, T. Wang, H. Zhang, Q. Xu, J. Yuan, Z. Li, Targeting microglia for therapy of Parkinson's disease by using biomimetic ultrasmall nanoparticles. *J. Am. Chem. Soc.* **142**, 21730–21742 (2020).
58. S. Xiong, Z. Li, Y. Liu, Q. Wang, J. Luo, X. Chen, Z. Xie, Y. Zhang, H. Zhang, T. Chen, Brain-targeted delivery shuttled by black phosphorus nanostructure to treat Parkinson's disease. *Biomaterials* **260**, 120339 (2020).
59. L. M. Jørgensen, T. Henriksen, S. Mardosiene, O. Wyon, S. H. Keller, B. Jespersen, G. M. Knudsen, D. S. Stenbæk, Hot and cold cognitive disturbances in Parkinson patients treated with DBS-STN: A combined PET and neuropsychological study. *Brain Sci.* **12**, 654 (2022).
60. M. Jahanshahi, F. Leimbach, V. Rawji, Short and long-term cognitive effects of subthalamic deep brain stimulation in Parkinson's disease and identification of relevant factors. *J. Parkinsons Dis.* **12**, 2191–2209 (2022).
61. M. Bucur, C. Papagno, Deep brain stimulation in Parkinson disease: A meta-analysis of the long-term neuropsychological outcomes. *Neuropsychol. Rev.* **33**, 307–346 (2023).
62. A. M. Strutt, R. Simpson, J. Jankovic, M. K. York, Changes in cognitive-emotional and physiological symptoms of depression following STN-DBS for the treatment of Parkinson's disease. *Eur. J. Neurol.* **19**, 121–127 (2011).
63. A. C. Sutton, W. Yu, M. E. Calos, A. B. Smith, A. Ramirez-Zamora, E. S. Molho, J. G. Pilitsis, J. M. Brotchie, D. S. Shin, Deep brain stimulation of the substantia nigra pars reticulata improves forelimb akinesia in the hemiparkinsonian rat. *J. Neurophysiol.* **109**, 363–374 (2013).
64. D. Weiss, S. Breit, T. Wächter, C. Plewnia, A. Gharabaghi, R. Krüger, Combined stimulation of the substantia nigra pars reticulata and the subthalamic nucleus is effective in hypokinetic gait disturbance in Parkinson's disease. *J. Neurol.* **258**, 1183–1185 (2011).
65. M. Heilbronn, M. Scholten, C. Schlenstedt, M. Mancini, A. Schöllmann, I. Cebi, M. Pötter-Nerger, A. Gharabaghi, D. Weiss, Anticipatory postural adjustments are modulated by substantia nigra stimulation in people with Parkinson's disease and freezing of gait. *Parkinsonism Relat. Disord.* **66**, 34–39 (2019).
66. I. Corripio, A. Roldán, P. McKenna, S. Sarró, A. Alonso-Solís, L. Salgado, E. Álvarez, J. Molet, E. Pomarol-Clotet, M. Portella, Target selection for deep brain stimulation in treatment resistant schizophrenia. *Prog. Neuropsychopharmacol. Biol. Psychiatry* **112**, 110436 (2022).
67. K. Eom, J. Kim, J. M. Choi, T. Kang, J. W. Chang, K. M. Byun, S. B. Jun, S. J. Kim, Enhanced infrared neural stimulation using localized surface plasmon resonance of gold nanorods. *Small* **10**, 3853–3857 (2014).
68. J. Yong, K. Needham, W. G. A. Brown, B. A. Nayagam, S. L. McArthur, A. Yu, P. R. Stoddart, Gold-nanorod-assisted near-infrared stimulation of primary auditory neurons. *Adv. Funct. Mater.* **3**, 1862–1868 (2014).
69. F. Gaven, P. Marin, S. Claeysen, Primary culture of mouse dopaminergic neurons. *J. Vis. Exp.* **91**, e51751 (2014).
70. T. Fath, Y. D. Ke, P. Gunning, J. Gotz, L. M. Ittner, Primary support cultures of hippocampal and substantia nigra neurons. *Nat. Protoc.* **4**, 78–85 (2009).
71. J. Park, K. Jin, A. Sahasrabudhe, P. H. Chiang, J. H. Maalouf, F. Koehler, D. Rosenfeld, S. Rao, T. Tanaka, T. Khudiyev, Z. J. Schiffer, Y. Fink, O. Yizhar, K. Manthiram, P. Anikeeva, In situ electrochemical generation of nitric oxide for neuronal modulation. *Nat. Nanotechnol.* **15**, 690–697 (2020).
72. Y.-R. Peng, S.-Y. Zeng, H.-L. Song, M.-Y. Li, M. K. Yamada, X. Yu, Postsynaptic spiking homeostatically induces cell-autonomous regulation of inhibitory inputs via retrograde signaling. *J. Neurosci.* **30**, 16220–16231 (2010).
73. X. Wang, X. Cui, J. Wu, L. Bao, Z. Tan, C. Chen, Peripheral nerves directly mediate the transneuronaltranslocation of silver nanomaterialsfrom the gut tocentral nervous system. *Sci. Adv.* **9**, eadg2252 (2023).

Acknowledgments: We thank X. Yu from Peking University McGovern Institute, Peking University, China for the discussion in therapeutic efficiency of ATB NP–based system. We thank Z. Y. Rao at Research Center for Eco-Environmental Sciences, Chinese Academy of Sciences for the assistance on confocal laser scanning microscopy and Q. Wang from State Key Laboratory of Natural and Biomimetic Drugs, Peking University, China for the assistance on binding affinity measurement. We thank ANATECH (Beijing) Co. Ltd. for the help with FSCV measurement. Figures were created with BioRender.com. **Funding:** This work was supported by the National Key Research and Development Program of China (grant nos. 2021YFA1200900 and 2022YFC2409701 to X.C. and C.C.), the National Natural Science Foundation of China (grant nos. 32271460 and 22388101 to X.C. and C.C.), the Youth Innovation Promotion Association of Chinese Academy of Sciences (grant no. 2023042 to X.C.), Beijing Nova Program (grant no. 20240484663 to X.C.), the Major Instrument Project of the National Natural Science Foundation of China (grant no. 22027810 to C.C.), and the New Cornerstone Science

Foundation (grant no. NCI202318 to C.C.). **Author contributions:** Conceptualization: J.W., X.C., and C.C. Investigation: J.W., L.B., and G.L. Writing—original draft: J.W. and X.C. Writing—review and editing: X.C. and C.C. Project administration: X.C. and C.C. Funding acquisition: X.C. and C.C. Supervision: X.C. and C.C. Methodology: J.W., X.C., L.B., and X.W. Resources: G.L. Validation: J.W. and G.L. Visualization: J.W. and X.C. Formal analysis: J.W., X.C., and G.L. **Competing interests:** The authors declare that they have no competing interests. **Data and materials availability:** All data needed to evaluate the conclusions in the paper are present in the paper and/or the Supplementary Materials. All the source data are accessible at Science Data Bank (https://cstr.cn/31253.11.sciencedb.18070).

Submitted 5 February 2024
Accepted 13 December 2024
Published 15 January 2025
10.1126/sciadv.ado4927